

# Linear stability analysis of Taylor bubble motion in downward flowing liquids in vertical tubes

## Supplementary information

H. A. Abubakar<sup>1,2</sup> and O. K. Matar<sup>1†</sup>

<sup>1</sup>Department of Chemical Engineering, Imperial College London, London SW7 2AZ, UK

<sup>2</sup>Department of Chemical Engineering, Ahmadu Bello University, Zaria 810107, Nigeria

(Received xx; revised xx; accepted xx)

### 1. Weak formulations

The transformation of the governing equations into their weak forms involves three steps: multiplying the governing equations for each variables with their corresponding *test functions* and integrating over the domain, integrating by part to reduce the order of integration, and, finally, incorporating the boundary conditions into the resulting relations. Before proceeding to derive the weak forms of the equations, it is important to define the necessary functional spaces to which the solution and test functions must belong (Heinrich & Pepper 1999):

(i) The  $L^2(\Omega)$  space: This is a space of functions  $f(\mathbf{r})$  defined in  $\Omega$  that are square integrable over  $\Omega$ :

$$L^2(\Omega) = \left\{ f(\mathbf{r}) \mid \int_{\Omega} (f(\mathbf{r}))^2 d\Omega < \infty \right\}. \quad (1.1)$$

(ii) The  $L_0^2(\Omega)$  subspace: This is a subspace of  $L^2(\Omega)$  defined in  $\Omega$  such that for functions defined in  $L^2(\Omega)$ , the following equation is satisfied:

$$L_0^2(\Omega) = \left\{ f \mid f \in L^2(\Omega) \text{ and } \int_{\Omega} f(\mathbf{r}) = 0 \right\}. \quad (1.2)$$

(iii) The Sobolev space  $H^1(\Omega)$ : this is a space of functions  $f(\mathbf{r})$  defined in  $\Omega$  such that both the function and all its first partial derivatives are in  $L^2(\Omega)$

$$H^1(\Omega) = \left\{ f(\mathbf{r}) \mid \int_{\Omega} [|f|^2 + |\nabla f|^2] d\Omega < \infty \right\}. \quad (1.3)$$

(iv) The Sobolev subspace  $H_0^1(\Omega)$ : this is a subspace of the Sobolev space  $H^1(\Omega)$  for which the functions defined in space  $H^1$  vanish on the portions of the boundary of  $\Omega$  where *Dirichlet* boundary conditions are imposed ( i.e  $\Gamma_D = \Gamma_{in} + \Gamma_{wall}$  ):

$$H_0^1(\Omega) = \{ f \mid f \in H^1(\Omega) \text{ and } f(\mathbf{r}) = \mathbf{0} \text{ if } \mathbf{r} \in \Gamma_D \}. \quad (1.4)$$

Let  $\Phi \in H_0^1$  and  $\varphi \in L_0^2$  be the test functions corresponding to  $\mathbf{u} \in H^1$  and  $p \in L^2$ , respectively. Next we take the inner product of momentum equation with  $\Phi$ , multiply

† Email address for correspondence: o.matar@imperial.ac.uk

continuity equation with  $\varphi$  and integrate the equations over the domain:

$$\int_{\Omega} \left\{ \frac{\partial \mathbf{u}}{\partial t} \cdot \Phi + [(\mathbf{u} \cdot \nabla) \mathbf{u}] \cdot \Phi - [\nabla \cdot \mathbf{T}] \cdot \Phi \right\} d\Omega = 0, \quad (1.5)$$

$$\int_{\Omega} \{(\nabla \cdot \mathbf{u}) \varphi\} d\Omega = 0. \quad (1.6)$$

Equations (1.5) and (1.6) are the weighted residual forms of the momentum and continuity equations, respectively. Integrating the last term on the left-hand-side of (1.5) by parts,

$$\int_{\Omega} \{[\nabla \cdot \mathbf{T}] \cdot \Phi\} d\Omega = \int_{\Gamma} \{\mathbf{n} \cdot \mathbf{T} \cdot \Phi\} d\Gamma_b - \int_{\Omega} \{\mathbf{T} : \nabla(\mathbf{u})\} d\Omega, \quad (1.7)$$

where

$$\Gamma = \Gamma_b + \Gamma_{in} + \Gamma_{wall} + \Gamma_{out}.$$

Enforcing the outlet boundary condition and taking into consideration that  $\Phi \in H_0^1$ , hence  $\Phi$  are zero where *essential* boundary conditions are imposed, we are left with

$$\Gamma = \Gamma_b.$$

Making use of the following expression for  $\mathbf{T}$ ,

$$\mathbf{T} = -p\mathbf{I} + N_f^{-1} (\nabla \mathbf{u} + \nabla \mathbf{u}^T) \quad (1.8)$$

(1.5) becomes

$$\int_{\Omega} \left\{ \frac{\partial \mathbf{u}}{\partial t} \cdot \Phi + [(\mathbf{u} \cdot \nabla) \mathbf{u}] \cdot \Phi + 2N_f^{-1} \mathbf{E}(\mathbf{u}) : \mathbf{E}(\Phi) - p(\nabla \cdot \Phi) \right\} d\Omega - \int_{\Gamma_b} \{\mathbf{n} \cdot \mathbf{T} \cdot \Phi\} d\Gamma_b = 0. \quad (1.9)$$

The traction term in the last term on the left-hand-side of (1.9) can be decomposed into its normal and tangential components (Pozrikidis 2011):

$$\mathbf{n} \cdot \mathbf{T} = [\mathbf{n} \cdot \mathbf{T} \cdot \mathbf{n}] \mathbf{n} + \mathbf{n} \times [\mathbf{n} \cdot \mathbf{T} \times \mathbf{n}], \quad (1.10)$$

thereby allowing the incorporation of normal stress condition and tangential stress condition into (1.9) to give

$$\int_{\Omega} \left\{ \frac{\partial \mathbf{u}}{\partial t} \cdot \Phi + [(\mathbf{u} \cdot \nabla) \mathbf{u}] \cdot \Phi + 2N_f^{-1} \mathbf{E}(\mathbf{u}) : \mathbf{E}(\Phi) - p(\nabla \cdot \Phi) \right\} d\Omega - \int_{\Gamma_b} \{[Eo^{-1}\kappa + z - P_b] \mathbf{n} \cdot \Phi\} d\Gamma_b = 0. \quad (1.11)$$

Equations (1.6) and (1.11) are the weak forms of the governing equations. Similarly for the kinematic boundary condition, we have

$$\int_{A_b} \left\{ \left[ \frac{d\mathbf{r}_b}{dt} \cdot \mathbf{n} - \mathbf{u} \cdot \mathbf{n} \right] \xi \right\} dA_b = 0. \quad (1.12)$$

where  $\mathbf{r}_b(t)$  represents the position vector for the location of the interface  $\Gamma_b^0$  and  $\xi$  denote the test functions for the interface deformation magnitude.

Table 1: Dimensionless parameters corresponding to the fluid properties used to validate the numerical predictions against the experimental work of Bugg & Saad (2002).

Fluid properties				Dimensionless parameters			
$\rho$ (kgm <sup>-3</sup> )	$\mu$ (Nsm <sup>-2</sup> )	$\gamma$ (Jm <sup>-2</sup> )	$v_b$ (m <sup>3</sup> )	$N_f$	$Eu$	$U_m$	$H_b$
911	$84 \times 10^{-3}$	$3.28 \times 10^{-2}$	$10 \times 10^{-6}$	88.95	98.33	0	2.00

## 2. Steady states: validation

The numerical method was validated by simulating the experiment of Bugg & Saad (2002) where the velocity field around a Taylor bubble rising in a stagnant olive oil in a pipe of diameter 19 mm was measured using Particle Image Velocimetry (PIV) at five different positions. The fluid properties used in the experiment and the corresponding dimensionless parameters are given in Table 1. In this table,  $H_b$  denotes the dimensionless equivalent height of pipe that the gas would occupy if it were to completely filled the pipe cross section. For the validation and the results discussed in the main article, a fixed dimensionless distance of  $L_a = 1.0$  and  $L_b = 4.5$  are maintained ahead and below the bubble nose, respectively. These distances and mesh structure were tested to ensure that the inlet and outlet boundaries as well as the mesh have insignificant influence on the steady-state results. The initial bubble shape and the converged steady-state bubble shape for the validation are shown in figures 3a and 3b of the main article.

The predicted dimensionless bubble rise speed is 0.2928, corresponding to a deviation of 3.4% from the experimentally measured value of 0.303. Further comparisons with the experiment were carried out using the flow field results at five measurement positions around the bubble. Ahead of the bubble, velocity measurements were taken along the pipe axis and in the radial direction at an axial distance of  $0.111D$ . figures 1a and 1b show the velocity profiles for these two locations and are well predicted by our simulation. figure 1c compares the velocity measurement taken at an axial distance of  $0.504D$  below the bubble nose. At this point, the magnitude of the radial velocity component is still developing. When the velocity in the film is fully-developed, the magnitude of the radial velocity at all points in the radial direction is approximately zero. By progressively plotting the radial velocity profile at various points below the bubble nose, a point is reached at which the radial velocity becomes zero. The axial velocity profile at this location is shown in figure 1d and the dimensionless film thickness was measured to be 0.1235. Although no experimental measurement of the film thickness was reported in Bugg & Saad (2002), the deviation of the numerical simulation results from the theoretical estimated value of Brown (1965) using (6.1), which predicts the film thickness to be 0.1193, is 3.52%.

As the liquid emerges from the falling film region into the wake of the bubble, the radial component of its velocity reappears in order to redirect the liquid from the film back towards the center of the pipe. Figure 1e shows the velocity profile in the wake of the Taylor bubble at an axial distance of  $0.2D$  below the bubble bottom and is also adequately well predicted.

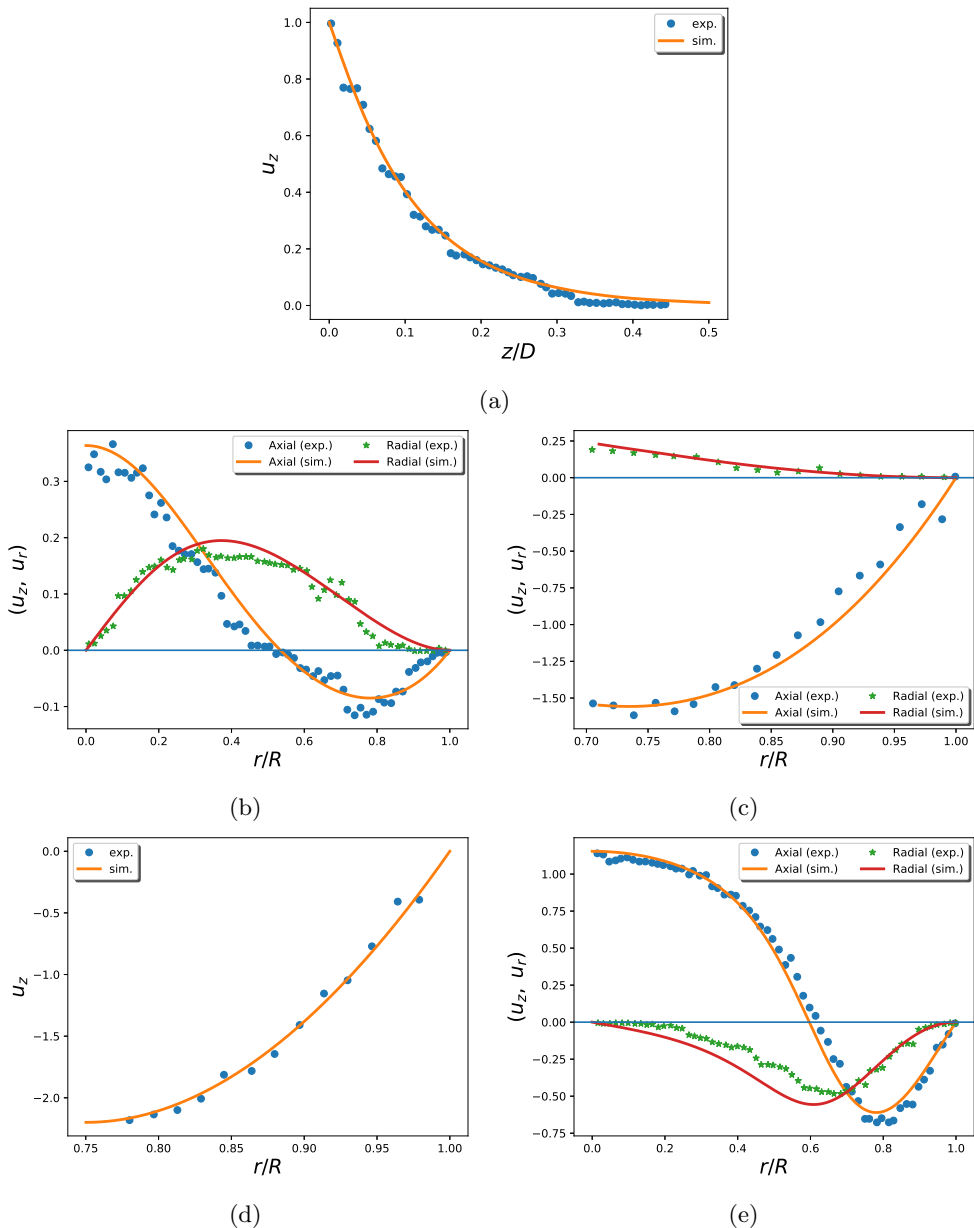


Figure 1: Validation of the numerical predictions (lines) for the velocity profiles for the positions indicated in Fig. 2 against the PIV measurements (symbols) of Bugg & Saad (2002); (a) dimensionless axial velocity component,  $u_z$ , along the pipe axis (position 1); (b) dimensionless axial,  $u_z$ , and radial,  $u_r$ , velocity components at  $\frac{z}{D} = 0.111$  ahead of the bubble nose (position 2); (c) dimensionless axial and radial velocity components in the developing film at  $\frac{z}{D} = 0.504$  below the bubble nose (position 3) and (d) dimensionless axial velocity component in the fully-developed film (position 4); (e) dimensionless axial and radial components of velocity at distance  $\frac{z}{D} = 0.20$  below the bubble bottom (position 5).

### 3. Curvature linearisation

For a three-dimensional axisymmetric surface, the interface location in any  $(r, z)$  plane is sufficient for computing the curvature of the surface. Consider that the interface in any such plane is spanned by a curve with the coordinates of any point on the curve being  $(r, z)$ . In addition, let the interface be parametrised by length of arc  $s$  so that the position vector of any point on the interface is given as

$$\mathbf{r} = r(s)\mathbf{i}_r + z(s)\mathbf{i}_z. \quad (3.1)$$

The total curvature at any given point on the interface is defined as

$$\kappa = -\nabla_s \cdot \mathbf{n}, \quad (3.2)$$

where  $r(s)$  and  $z(s)$  are the radial and axial coordinates of the points on the interface, respectively;  $\mathbf{n}$  remains the unit normal to the interface and  $\nabla_s$  is the surface tangential gradient operator which is given as

$$\nabla_s = (\mathbf{I} - \mathbf{n} \otimes \mathbf{n}) \nabla. \quad (3.3)$$

For a three-dimensional axisymmetric surface, (3.3) simplifies to

$$\nabla_s = t_r \frac{d}{ds} \mathbf{i}_r + \frac{1}{r} \frac{\partial}{\partial \theta} \mathbf{i}_\theta + t_z \frac{d}{ds} \mathbf{i}_z, \quad (3.4)$$

and (3.2) becomes

$$\kappa = - \left( \mathbf{t} \cdot \frac{d\mathbf{n}}{ds} + \frac{n_r}{r} \right), \quad (3.5)$$

where  $\mathbf{t}$  is the unit tangent vector to the interface with components  $t_r$ ,  $t_\theta$  and  $t_z$  in the radial, azimuthal and axial directions, respectively;  $\frac{d}{ds} = (\mathbf{t} \cdot \nabla)$  is an operator that denotes the derivative in the tangential direction;  $n_r$  is the radial component of the unit normal vector,  $\mathbf{n}$ .

Let us imagine that the deformed interface can be expressed as a summation of the undeformed interface and a very small deformation. Thus, the deformed interface can be written as

$$\mathbf{r} = \mathbf{r}^0 + \mathbf{x}, \quad (3.6)$$

where  $\mathbf{r}^0 = r^0 \mathbf{i}_r + \theta^0 \mathbf{i}_\theta + z^0 \mathbf{i}_z$  and  $\mathbf{r} = r \mathbf{i}_r + \theta \mathbf{i}_\theta + z \mathbf{i}_z$  are the undeformed (i.e base) and deformed (i.e perturbed) interface position vectors, respectively;  $\mathbf{x} = x_r \mathbf{i}_r + x_\theta \mathbf{i}_\theta + x_z \mathbf{i}_z$ , as mentioned in the previous section, is the interface deformation vector and is taken to be very small in magnitude. Linearisation of the unit normal to, and elemental arc length on, the deformed interface about the undeformed interface give (Krutz *et al.* 1988; Ramanan & Engelman 1996; Weatherburn 1927)

$$\mathbf{n} = \mathbf{n}^0 - \mathbf{n}^0 \times \nabla_s \times \mathbf{x}, \quad (3.7)$$

$$ds = \left( 1 + \mathbf{t}^0 \cdot \frac{d\mathbf{x}}{ds^0} \right) ds^0, \quad (3.8)$$

$$\frac{d}{ds} = \left( 1 - \mathbf{t}^0 \cdot \frac{d\mathbf{x}}{ds^0} \right) \frac{d}{ds^0}. \quad (3.9)$$

On further simplification of (3.7)

$$\mathbf{n} = \mathbf{n}^0 - \mathbf{t}^0 \left( \mathbf{n}^0 \cdot \frac{d\mathbf{x}}{ds^0} \right) - \frac{\mathbf{n}^0}{r^0} \cdot \frac{\partial \mathbf{x}}{\partial \theta^0} \mathbf{i}_\theta. \quad (3.10)$$

Substituting (4.5) together with (3.6) and (3.9) into (3.5), the linearised curvature neglecting all terms of nonlinear in  $x$  gives

$$\kappa = \kappa^0 + \kappa^1, \quad (3.11)$$

with

$$\kappa^0 = - \left( \mathbf{t}^0 \cdot \frac{d\mathbf{n}^0}{ds^0} + \frac{n_r^0}{r^0} \right), \quad (3.12)$$

$$\begin{aligned} \kappa^1 = \frac{1}{r^0} \frac{d}{ds^0} \left[ r^0 \left( \mathbf{n}^0 \cdot \frac{d\mathbf{x}}{ds^0} \right) \right] + 2 \left( \mathbf{t}^0 \cdot \frac{d\mathbf{x}}{ds^0} \right) \left( \mathbf{t}^0 \cdot \frac{d\mathbf{n}^0}{ds^0} \right) + \frac{\mathbf{n}^0}{r^{02}} \cdot \frac{\partial^2 \mathbf{x}}{\partial \theta^2} + \frac{x_r n_r^0}{r^{02}} \\ - \frac{d\mathbf{n}^0}{ds^0} \cdot \frac{d\mathbf{x}}{ds^0}. \end{aligned} \quad (3.13)$$

When (4.6) is further simplified by allowing the deformation vector to be of the form

$$\mathbf{x} = h\mathbf{n}^0, \quad (3.14)$$

it results in

$$\kappa^1 = \frac{1}{r^0} \frac{d}{ds^0} \left( r^0 \frac{dh}{ds^0} \right) + h \left[ \kappa_a^{02} + \kappa_b^{02} + \frac{1}{r^{02}} \frac{\partial^2 h}{\partial \theta^2} \right], \quad (3.15)$$

which is the same as the expression derived for curvature perturbation in Chireux *et al.* (2015), albeit through a different and longer route. In arriving at (3.15), we have used the following Frenet-Serret relations

$$\frac{d\mathbf{t}}{ds} = \kappa\mathbf{n}, \quad (3.16a)$$

$$\frac{d\mathbf{n}}{ds} = -\kappa\mathbf{t}. \quad (3.16b)$$

Equations (3.13) and (3.15) are the expressions for curvature deformation and can be used for an axisymmetric deformation by setting the term containing derivative with respect to the azimuthal coordinate to zero to obtain

$$\kappa^1 = \frac{1}{r^0} \frac{d}{ds^0} \left( r^0 \frac{dh}{ds^0} \right) + h \left[ \kappa_a^{02} + \kappa_b^{02} \right]. \quad (3.17)$$

In (3.7)-(3.15),  $\mathbf{n}^0$  is the unit normal vector to the undeformed interface and  $n_r^0$ ,  $n_\theta^0$  and  $n_z^0$  are its component in the radial, azimuthal and axial directions, respectively;  $\mathbf{t}^0$  is the unit tangent vector to the undeformed interface with components  $t_r^0$ ,  $t_\theta^0$  and  $t_z^0$  in the radial, azimuthal and axial directions, respectively;  $ds$  and  $ds^0$  are the elemental arc length for the deformed and undeformed interfaces, respectively;  $\kappa^0$  is the curvature of the undeformed surface and  $\kappa^1$  is the addition to the undeformed interface curvature (also referred to as curvature perturbation in the context of linear stability analysis) due to linearisation of the deformed interface about the undeformed interface;  $h$  is the magnitude of the interface deformation in the direction normal to the undeformed interface.  $\kappa_a^0$  and  $\kappa_b^0$  are the two principal curvatures of the undeformed interface (3.12) corresponding to the curvature in the  $r - z$  and  $r - \theta$  planes, respectively, defined as

$$\kappa_a^0 = \mathbf{t}^0 \cdot \frac{d\mathbf{n}^0}{ds^0}, \quad (3.18a)$$

$$\kappa_b^0 = \frac{n_r^0}{r^0}. \quad (3.18b)$$

#### 4. Development of perturbation equation model and eigenvalue problem

We begin the model development from the derived weak forms of the continuity, momentum and kinematic boundary conditions equations, (1.6), (1.11) and (1.12). Similar to domain perturbation, we assume that the three-dimensional base flow domain is perturbed by the addition of infinitesimal deformation field  $\tilde{\mathbf{x}}$  to its position vector and that (1.6), (1.11) and (1.12) are valid on the three-dimensional perturbed domain.

Let the position vector of the perturbed domain be written as

$$\mathbf{r} = \mathbf{r}^0 + \epsilon \tilde{\mathbf{x}}, \quad (4.1)$$

where  $\mathbf{r}^0 = (r^0, \theta^0, z^0)$  represents the position vector of the unperturbed three-dimensional base flow domain,  $\tilde{\mathbf{x}} = (\tilde{x}_r, \tilde{x}_\theta, \tilde{x}_z)$  is a deformation field defined over the entire base flow domain, and  $\epsilon \ll 1$  to signify the infinitesimally small nature of the applied perturbations. The linearised elemental volume of the perturbed three-dimensional domain is given as (Cairncross *et al.* 2000; Carvalho & Scriven 1999)

$$\begin{aligned} dV &= r dr d\theta dz = (1 + \nabla \cdot \tilde{\mathbf{x}}) r^0 dr^0 d\theta^0 dz^0 \\ &= (1 + \nabla \cdot \tilde{\mathbf{x}}) d\Omega^0 d\theta^0; \end{aligned} \quad (4.2)$$

thus, we can relate the elemental volume in the perturbed three-dimensional domain to the base flow two-dimensional axisymmetric domain,  $d\Omega^0 = r^0 dr^0 dz^0$ . Similarly, an elemental area on the perturbed interface in the three-dimensional domain,  $dA_b$ , can be related to base flow length of arc,  $\Gamma_b^0$  in the two-dimensional axisymmetric domain:

$$dA_b = (1 + \nabla_s \cdot \tilde{\mathbf{x}}) d\Gamma_b^0 d\theta^0, \quad (4.3)$$

where  $\nabla_s$  is the surface gradient operator; the interface terms can be linearised as follows

$$\mathbf{n} = \mathbf{n}^0 + \epsilon \tilde{\mathbf{n}}, \quad (4.4a)$$

$$\kappa = \kappa^0 + \epsilon \tilde{\kappa}, \quad (4.4b)$$

$$\Phi = \Phi + \epsilon (\tilde{\mathbf{x}} \cdot \nabla) \Phi, \quad (4.4c)$$

$$\mathbf{u} = \mathbf{u} + \epsilon (\tilde{\mathbf{x}} \cdot \nabla) \mathbf{u}; \quad (4.4d)$$

here,  $\mathbf{n}^0$  and  $\kappa^0$  are the base state interface normal vector and curvature, and  $\tilde{\mathbf{n}}$  and  $\tilde{\kappa}$  represent the normal vector and curvature perturbations, respectively (see section 3):

$$\tilde{\mathbf{n}} = -\mathbf{t}^0 \left( \mathbf{n}^0 \cdot \frac{d\tilde{\mathbf{x}}}{ds^0} \right) - \frac{\mathbf{n}^0}{r^0} \cdot \frac{\partial \tilde{\mathbf{x}}}{\partial \theta^0}, \mathbf{i}_\theta \quad (4.5)$$

$$\begin{aligned} \tilde{\kappa} &= \frac{1}{r^0} \frac{d}{ds^0} \left[ r^0 \left( \mathbf{n}^0 \cdot \frac{d\tilde{\mathbf{x}}}{ds^0} \right) \right] + 2 \left( \mathbf{t}^0 \cdot \frac{d\tilde{\mathbf{x}}}{ds^0} \right) \left( \mathbf{t}^0 \cdot \frac{d\mathbf{n}^0}{ds^0} \right) \\ &\quad + \frac{\mathbf{n}^0}{r^{02}} \cdot \frac{\partial^2 \tilde{\mathbf{x}}}{\partial \theta^0^2} + \frac{\tilde{x}_r n_r^0}{r^{02}} - \frac{d\mathbf{n}^0}{ds^0} \cdot \frac{d\tilde{\mathbf{x}}}{ds^0}, \end{aligned} \quad (4.6)$$

where  $\frac{d}{ds^0} = \mathbf{t} \cdot \nabla$  is the derivative along the arc length  $s$  on the base state interface. Substitution into (1.6), (1.11) and (1.12) of (4.1)-(4.4), together with the flow field perturbations

$$\mathbf{u} = \mathbf{u}^0 + \epsilon \tilde{\mathbf{u}}, \quad (4.7a)$$

$$p = p^0 + \epsilon \tilde{p}, \quad (4.7b)$$

followed by neglecting all terms of order  $\epsilon^2$  respectively yields the following leading order momentum, continuity, and kinematic condition equations

$$\int_0^{2\pi} \left\{ \int_{\Omega^0} \{ [(\mathbf{u}^0 \cdot \nabla) \mathbf{u}^0] \cdot \Phi + 2N_f^{-1} \mathbf{E}(\mathbf{u}^0) : \mathbf{E}(\Phi) - p^0 (\nabla \cdot \Phi) \} d\Omega^0 - \int_{\Gamma_b^0} \{ [Eo^{-1} \kappa^0 + z^0 - P_b^0] \mathbf{n}^0 \cdot \Phi \} d\Gamma_b^0 \right\} d\theta^0 = 0, \quad (4.8)$$

$$\int_0^{2\pi} \int_{\Omega^0} \{ \{ (\nabla \cdot \mathbf{u}^0) \varphi \} [1 + \nabla \cdot \tilde{\mathbf{x}}] \} d\Omega^0 d\theta^0 = 0, \quad (4.9)$$

$$\int_0^{2\pi} \int_{\Gamma_b^0} \left\{ \left\{ \left[ \frac{d\mathbf{x}_b^0}{dt} \cdot \mathbf{n}^0 - \mathbf{u}^0 \cdot \mathbf{n}^0 \right] \xi \right\} [1 + \nabla_s \cdot \tilde{\mathbf{x}}] \right\} d\Gamma_b^0 d\theta^0 = 0. \quad (4.10)$$

It is also possible to write the following equations at  $O(\epsilon)$  to yield equations that feature the perturbation variables: the momentum conservation equation,

$$\begin{aligned} & \int_0^{2\pi} \int_{\Omega^0} \left\{ \frac{\partial \tilde{\mathbf{u}}}{\partial t} \cdot \Phi + [(\mathbf{u}^0 \cdot \nabla) \tilde{\mathbf{u}} + (\tilde{\mathbf{u}} \cdot \nabla) \mathbf{u}^0] \cdot \Phi + 2N_f^{-1} \mathbf{E}(\tilde{\mathbf{u}}) : \mathbf{E}(\Phi) \right\} d\Omega^0 d\theta^0 \\ & - \int_0^{2\pi} \int_{\Omega^0} \{ \tilde{p} (\nabla \cdot \Phi) \} d\Omega^0 d\theta^0 \\ & - \int_0^{2\pi} \int_{\Gamma_b^0} \{ [Eo^{-1} \tilde{\kappa} + \tilde{z}] \mathbf{n}^0 \cdot \Phi \} d\Gamma_b^0 d\theta^0 \\ & + \int_0^{2\pi} \int_{\Gamma_b^0} \tilde{\mathbf{x}} \cdot \mathbf{n}^0 \{ [(\mathbf{u}^0 \cdot \nabla) \mathbf{u}^0] \cdot \Phi + 2N_f^{-1} \mathbf{E}(\mathbf{u}^0) : \mathbf{E}(\Phi) - p^0 (\nabla \cdot \Phi) \} d\Gamma_b^0 d\theta^0 \\ & - \int_0^{2\pi} \int_{\Gamma_b^0} \{ [Eo^{-1} \kappa^0 + z^0 - P_b^0] [\tilde{\mathbf{n}} \cdot \Phi + [(\tilde{\mathbf{x}} \cdot \nabla) \Phi] \cdot \mathbf{n}^0 + (\nabla_s \cdot \tilde{\mathbf{x}}) \mathbf{n}^0 \cdot \Phi] \} d\Gamma_b^0 d\theta^0 \\ & = 0, \end{aligned} \quad (4.11)$$

where  $\mathbf{u}^0$ ,  $p^0$ , and  $P_b^0$  represent the base flow solutions for the variables; and  $\tilde{\mathbf{u}}$  and  $\tilde{p}$  denote the perturbations to the flow field variables, and the last two lines of (4.11) are due to the linearisation of the domain and boundary terms of (1.11) where we have used Gauss's divergence theorem to restrict the deformation to the interface as it is expected in classical linear stability formulation; the continuity equation,

$$\int_0^{2\pi} \int_{\Omega^0} \{ (\nabla \cdot \tilde{\mathbf{u}}) \varphi \} d\Omega^0 d\theta^0 = 0, \quad (4.12)$$

and the kinematic condition:

$$\int_0^{2\pi} \int_{\Gamma_b^0} \left\{ \left[ \frac{d\tilde{\mathbf{x}}}{dt} \cdot \mathbf{n}^0 - \tilde{\mathbf{u}} \cdot \mathbf{n}^0 - \mathbf{u}^0 \cdot \tilde{\mathbf{n}} - [(\tilde{\mathbf{x}} \cdot \nabla) \mathbf{u}^0] \cdot \mathbf{n}^0 \right] \xi \right\} d\Gamma_b^0 d\theta^0 = 0. \quad (4.13)$$

Simplifying (4.11)-(4.13) further by substituting for  $\tilde{\mathbf{n}}$  and  $\tilde{\kappa}$  using (4.5) and (4.6), respectively, and taking the deformation field to be of the form  $\tilde{\mathbf{x}} = \tilde{h} \mathbf{n}^0$ , since the deformation has been restricted to the interface and making use of the relations

$$\mathbf{u}^0 = (\mathbf{u}^0 \cdot \mathbf{n}^0) \mathbf{n}^0 + (\mathbf{u}^0 \cdot \mathbf{t}^0) \mathbf{t}^0, \quad (4.14a)$$

$$\nabla = (\mathbf{I} - \mathbf{n}^0 \otimes \mathbf{n}^0) \cdot \nabla + (\mathbf{n}^0 \otimes \mathbf{n}^0) \cdot \nabla, \quad (4.14b)$$

(4.11)-(4.13), after some algebra, can be expressed as follows

$$\begin{aligned}
& \int_0^{2\pi} \int_{\Omega^0} \left\{ \frac{\partial \tilde{\mathbf{u}}}{\partial t} \cdot \Phi + [(\mathbf{u}^0 \cdot \nabla) \tilde{\mathbf{u}} + (\tilde{\mathbf{u}} \cdot \nabla) \mathbf{u}^0] \cdot \Phi + 2N_f^{-1} \mathbf{E}(\tilde{\mathbf{u}}) : \mathbf{E}(\Phi) \right\} d\Omega^0 d\theta \\
& - \int_0^{2\pi} \int_{\Omega^0} \{ \tilde{p}(\nabla \cdot \Phi) \} d\Omega^0 d\theta \\
& - \int_0^{2\pi} \int_{\Gamma_b^0} Eo^{-1} \left\{ -\frac{d\tilde{h}}{ds} \left[ \mathbf{n} \cdot \frac{d\Phi}{ds} - \kappa_a(\mathbf{t} \cdot \Phi) \right] + \left[ \tilde{h}(\kappa_a^2 + \kappa_b^2) + \frac{1}{r^2} \frac{\partial^2 \tilde{h}}{\partial \theta^2} \right] \mathbf{n} \cdot \Phi \right\} d\Gamma_b^0 d\theta \\
& - \int_0^{2\pi} \int_{\Gamma_b^0} \{ \tilde{h} n_z(\mathbf{n} \cdot \Phi) \} d\Gamma_b^0 d\theta \\
& + \int_0^{2\pi} \int_{\Gamma_b^0} \tilde{h} \left\{ (\mathbf{u}^0 \cdot \mathbf{t}) \left[ \frac{d\mathbf{u}^0}{ds} \cdot \Phi \right] + \left[ -p^0 + 2N_f^{-1} \left( \mathbf{t} \cdot \frac{d\mathbf{u}^0}{ds} \right) \right] \left( \mathbf{t} \cdot \frac{d\Phi}{ds} \right) \right. \\
& + \left. \left[ -p^0 + 2N_f^{-1} \frac{u_r^0}{r} \right] \left( \frac{\Phi_r}{r} + \frac{1}{r} \frac{\partial \Phi_\theta}{\partial \theta} \right) \right\} d\Gamma_b^0 d\theta \\
& + \int_0^{2\pi} \int_{\Gamma_b^0} \left\{ [Eo^{-1} \kappa + z - P_b^0] \left[ (\mathbf{t} \cdot \Phi) \frac{d\tilde{h}}{ds} + \frac{\Phi_\theta}{r} \frac{\partial \tilde{h}}{\partial \theta} + \tilde{h} \kappa(\mathbf{n} \cdot \Phi) \right] \right\} d\Gamma_b^0 d\theta = 0, \tag{4.15}
\end{aligned}$$

$$\int_0^{2\pi} \int_{\Omega^0} \{ (\nabla \cdot \tilde{\mathbf{u}}) \varphi \} d\Omega d\theta = 0, \tag{4.16}$$

$$\int_0^{2\pi} \int_{\Gamma_b^0} \left\{ \left[ \frac{d\tilde{h}}{dt} - \tilde{\mathbf{u}} \cdot \mathbf{n} + (\mathbf{u}^0 \cdot \mathbf{t}) \frac{d\tilde{h}}{ds} - \tilde{h} \left( \frac{d\mathbf{u}^0}{dn} \cdot \mathbf{n} \right) \right] \xi \right\} d\Gamma_b^0 d\theta = 0, \tag{4.17}$$

where  $\frac{d}{dn} = (\mathbf{n} \cdot \nabla)$  is the derivative in the normal direction. Equations (4.15)-(4.17) are the perturbation equations for the linear analysis and in them we have suppressed the use of the superscript ‘0’ to designate base state quantities for the unit tangent and normal vectors for the sake of brevity.

We now transformed the perturbation equations to normal mode forms by assuming the following forms for the perturbation variables:

$$\tilde{\mathbf{u}}(r, \theta, z, t) = \hat{\mathbf{u}}(r, z) e^{(im\theta + \beta t)}, \tag{4.18a}$$

$$\tilde{p}(r, \theta, z, t) = \hat{p}(r, z) e^{(im\theta + \beta t)}, \tag{4.18b}$$

$$\tilde{h}(s, \theta, t) = \hat{h}(s) e^{(im\theta + \beta t)}, \tag{4.18c}$$

and their corresponding test functions as

$$\Phi(r, \theta, z) = \bar{\Phi}(r, z) e^{(-im\theta)}, \tag{4.19a}$$

$$\varphi(r, \theta, z) = \bar{\varphi}(r, z) e^{(-im\theta)}, \tag{4.19b}$$

$$\xi(s, \theta) = \bar{\xi}(s) e^{(-im\theta)}, \tag{4.19c}$$

where  $\hat{\mathbf{u}}$ ,  $\hat{p}$ , and  $\hat{h}$  are complex functions of space representing the amplitude of the velocity, pressure, and interface deformation perturbations, respectively;  $m$  is a dimensionless (integer) wave number in the azimuthal direction  $\theta$ ;  $\beta = \beta_R + i\beta_I$  is the complex growth rate which can be decomposed into its real  $\beta_R$  and imaginary  $\beta_I$  parts denoting the temporal growth rate and frequency, respectively: if  $\beta_R$  is positive (negative), the disturbance grows (decays) exponentially in time and the base

flow is linearly unstable (stable); if  $\beta_R$  is zero, the disturbance is neutrally stable. Substituting (4.18) and (4.19) into (4.15)-(4.17), separating the momentum equation into its components, yields the following equations governing the normal mode evolution of the perturbations as a function of  $N_f$ ,  $EO$ ,  $U_m$ , and  $m$ :

$$\begin{aligned}
& \int_{\Omega^0} \left\{ \beta \hat{u}_r \bar{\Phi}_r + \left[ \hat{u}_r \frac{\partial u_r^0}{\partial r} + \hat{u}_z \frac{\partial u_r^0}{\partial z} + u_r^0 \frac{\partial \hat{u}_r}{\partial r} + u_z^0 \frac{\partial \hat{u}_r}{\partial z} \right] \bar{\Phi}_r + N_f^{-1} \left[ 2 \frac{\partial \hat{u}_r}{\partial r} \frac{\partial \bar{\Phi}_r}{\partial r} \right. \right. \\
& \quad \left. \left. + (2 + m^2) \frac{\hat{u}_r \bar{\Phi}_r}{r^2} + 3im \frac{\hat{u}_\theta \bar{\Phi}_r}{r^2} - im \frac{\bar{\Phi}_r}{r} \frac{\partial \hat{u}_\theta}{\partial r} + \frac{\partial \bar{\Phi}_r}{\partial z} \left( \frac{\partial \hat{u}_r}{\partial z} + \frac{\partial \hat{u}_z}{\partial r} \right) \right] \right. \\
& \quad \left. - \hat{p} \left( \frac{\partial \bar{\Phi}_r}{\partial r} + \frac{\bar{\Phi}_r}{r} \right) \right\} d\Omega^0 \\
& - \int_{\Gamma_b^0} EO^{-1} \left\{ -\frac{d\hat{h}}{ds} \left[ n_r \frac{d\bar{\Phi}_r}{ds} - \kappa_a (t_r \bar{\Phi}_r) \right] + \hat{h} \left[ \kappa_a^2 + \kappa_b^2 - \frac{m^2}{r^2} \right] n_r \bar{\Phi}_r \right\} d\Gamma_b^0 \\
& - \int_{\Gamma_b^0} \left\{ \hat{h} n_z (n_r \bar{\Phi}_r) \right\} d\Gamma_b^0 \\
& + \int_{\Gamma_b^0} \hat{h} \left\{ (u_r^0 t_r) \left[ \frac{du_r^0}{ds} \bar{\Phi}_r \right] + \left[ -p^0 + 2N_f^{-1} \left( t_r \frac{du_r^0}{ds} \right) \right] \left( t_r \frac{d\bar{\Phi}_r}{ds} \right) \right. \\
& \quad \left. + \left[ -p^0 + 2N_f^{-1} \frac{u_r^0}{r} \right] \left( \frac{\bar{\Phi}_r}{r} \right) \right\} d\Gamma_b^0 \\
& + \int_{\Gamma_b^0} \left\{ [EO^{-1} \kappa + z - P_b^0] \left[ (t_r \bar{\Phi}_r) \frac{d\hat{h}}{ds} + \hat{h} \kappa (n_r \bar{\Phi}_r) \right] \right\} d\Gamma_b^0 = 0, \tag{4.20}
\end{aligned}$$

$$\begin{aligned}
& \int_{\Omega^0} \left\{ \beta \hat{u}_\theta \bar{\Phi}_\theta + \left[ u_r^0 \frac{\partial \hat{u}_\theta}{\partial r} + u_z^0 \frac{\partial \hat{u}_\theta}{\partial z} + \frac{u_r^0 \hat{u}_\theta}{r} \right] \bar{\Phi}_\theta + N_f^{-1} \left[ (1 + 2m^2) \frac{\hat{u}_\theta \bar{\Phi}_\theta}{r^2} + \frac{\partial \hat{u}_\theta}{\partial z} \frac{\partial \bar{\Phi}_\theta}{\partial z} \right. \right. \\
& \quad \left. \left. + \frac{\partial \hat{u}_\theta}{\partial r} \frac{\partial \bar{\Phi}_\theta}{\partial r} - \left( \frac{\hat{u}_\theta}{r} \frac{\partial \bar{\Phi}_\theta}{\partial r} + \frac{\bar{\Phi}_\theta}{r} \frac{\partial \hat{u}_\theta}{\partial r} \right) + im \left( \frac{\hat{u}_r}{r} \frac{\partial \bar{\Phi}_\theta}{\partial r} + \frac{\hat{u}_z}{r} \frac{\partial \bar{\Phi}_\theta}{\partial z} \right) - 3im \frac{\hat{u}_r \bar{\Phi}_\theta}{r^2} \right] \right. \\
& \quad \left. - p \left( -im \frac{\bar{\Phi}_\theta}{r} \right) \right\} d\Omega^0 + \int_{\Gamma_b^0} \hat{h} \left\{ \left[ -p^0 + 2N_f^{-1} \frac{u_r^0}{r} \right] \left( -im \frac{\bar{\Phi}_\theta}{r} \right) \right\} d\Gamma_b^0 \\
& + \int_{\Gamma_b^0} \left\{ \hat{h} [EO^{-1} \kappa + z - P_b^0] \left[ im \frac{\bar{\Phi}_\theta}{r} \right] \right\} d\Gamma_b^0 = 0, \tag{4.21}
\end{aligned}$$

$$\begin{aligned}
& \int_{\Omega^0} \left\{ \beta \hat{u}_z \bar{\Phi}_z + \left[ \hat{u}_r \frac{\partial u_z^0}{\partial r} + \hat{u}_z \frac{\partial u_z^0}{\partial z} + u_r^0 \frac{\partial \hat{u}_z}{\partial r} + u_z^0 \frac{\partial \hat{u}_z}{\partial z} \right] \bar{\Phi}_z + N_f^{-1} \left[ 2 \frac{\partial \hat{u}_z}{\partial z} \frac{\partial \bar{\Phi}_z}{\partial z} + m^2 \frac{\hat{u}_z \bar{\Phi}_z}{r^2} \right. \right. \\
& \quad \left. \left. - im \frac{\bar{\Phi}_z}{r} \frac{\partial \hat{u}_\theta}{\partial z} + \frac{\partial \bar{\Phi}_z}{\partial r} \left( \frac{\partial \hat{u}_r}{\partial z} + \frac{\partial \hat{u}_z}{\partial r} \right) \right] - \hat{p} \left( \frac{\partial \bar{\Phi}_z}{\partial z} \right) \right\} d\Omega^0 \\
& - \int_{\Gamma_b^0} Eo^{-1} \left\{ -\frac{d\hat{h}}{ds} \left[ n_z \frac{d\bar{\Phi}_z}{ds} - \kappa_a (t_z \bar{\Phi}_z) \right] + \hat{h} \left[ \kappa_a^2 + \kappa_b^2 - \frac{m^2}{r^2} \right] n_z \bar{\Phi}_z \right\} d\Gamma_b^0 \\
& - \int_{\Gamma_b^0} \left\{ \hat{h} n_z (n_z \bar{\Phi}_z) \right\} d\Gamma_b^0 \\
& + \int_{\Gamma_b^0} \hat{h} \left\{ (u_z^0 t_z) \left[ \frac{du_z^0}{ds} \bar{\Phi}_z \right] + \left[ -p^0 + 2N_f^{-1} \left( t_z \frac{du_z^0}{ds} \right) \right] \left( t_z \frac{d\bar{\Phi}_z}{ds} \right) \right\} d\Gamma_b^0 \\
& + \int_{\Gamma_b^0} \left\{ [Eo^{-1} \kappa + z - P_b^0] \left[ (t_z \bar{\Phi}_z) \frac{d\hat{h}}{ds} + \hat{h} \kappa (n_z \bar{\Phi}_z) \right] \right\} d\Gamma_b^0 = 0, \tag{4.22}
\end{aligned}$$

$$\int_{\Omega^0} \left\{ \left[ \frac{\partial \hat{u}_r}{\partial r} + \frac{\hat{u}_r}{r} - im \frac{\hat{u}_\theta}{r} + \frac{\partial \hat{u}_z}{\partial z} \right] \bar{\varphi} \right\} d\Omega^0 = 0, \tag{4.23}$$

$$\int_{\Gamma_b^0} \left\{ \left[ \beta \hat{h} - \hat{\mathbf{u}} \cdot \mathbf{n} + (\mathbf{u}^0 \cdot \mathbf{t}) \frac{d\hat{h}}{ds} - \hat{h} \left( \frac{d\mathbf{u}^0}{dn} \cdot \mathbf{n} \right) \right] \bar{\xi} \right\} d\Gamma_b^0 = 0. \tag{4.24}$$

The combined finite element forms for the perturbations (4.20)-(4.24) can be recast as a generalised eigenvalue problem

$$\beta \mathbf{B} \mathbf{y} = \mathbf{J} \mathbf{y}, \tag{4.25}$$

with  $\beta$  being the eigenvalue,  $\mathbf{B}$  the mass matrix,  $\mathbf{y}$  the eigenfunctions, and  $\mathbf{J}$  the Jacobian matrix.

The boundary conditions at the inlet, wall, and outlet reduce to the following conditions on the perturbations:

$$\hat{\mathbf{u}} = \mathbf{0} \quad \text{on} \quad \Gamma_{in}^0 \quad \text{and} \quad \Gamma_{wall}^0, \tag{4.26}$$

$$\mathbf{n} \cdot \hat{\mathbf{T}} \cdot \mathbf{n} = 0 \quad \text{and} \quad (\mathbf{I} - \mathbf{n} \otimes \mathbf{n}) \cdot \hat{\mathbf{u}} = 0 \quad \text{on} \quad \Gamma_{out}^0, \tag{4.27}$$

where the tensor  $\hat{\mathbf{T}}$  is expressed by

$$\hat{\mathbf{T}} = -\hat{p} + 2N_f^{-1} \hat{\mathbf{E}}(\hat{\mathbf{u}}); \quad \hat{\mathbf{E}}(\hat{\mathbf{u}}) = \frac{1}{2} \left[ \nabla \hat{\mathbf{u}} + \nabla \hat{\mathbf{u}}^T \right].$$

We stress that while it is customary to impose additional conditions along the axis of symmetry  $\Gamma_{sym}^0$ , we did not apply any such conditions in this case because the model equations were written around the perturbed three-dimensional domain and then linearised before integrating out the  $\theta$  dependence.

## 5. Linear stability: validation

We test the validity of our linear stability model and its numerical solution procedure by examining the stability of a spherical bubble of fixed volume in a stagnant liquid with negligible gravitational and boundary effects. The bubble is stable under these conditions and its motion is governed by an analytical solution (Miller & Scriven 1968; Prosperetti 1980). We compare our numerical results for the eigenvalues with this solution given in Prosperetti (1980) for small amplitude normal mode perturbations. The characteristic

scales used for the non-dimensionalisation of space, velocity, and pressure in the governing equations are  $R$ ,  $\sqrt{\gamma/(\rho R)}$ , and  $\gamma/R$ , respectively, where  $R$  is the bubble radius, so that the validation problem is parameterised by the Ohnesorge number,  $Oh = \mu/\sqrt{\rho R \gamma}$ .

Based on the scaling above, the dimensionless form of the characteristic equation for the bubble oscillations reads (Prosperetti 1980)

$$\left[ \mathcal{H}_{m-\frac{1}{2}}^{(1)}(X^*) \right] \beta^2 + Oh \left[ 4m(m+2)^2 - 2(m+2)(2m+1)(\mathcal{H}_{m-\frac{1}{2}}^{(1)}(X^*) + 2) \right] \beta + (m+1)(m-1)(m+2)(\mathcal{H}_{m-\frac{1}{2}}^{(1)}(X^*) + 2) = 0, \quad (5.1)$$

where  $X^*$  is a rescaled growth rate, and  $\mathcal{H}_j^{(1)}(X^*)$  is a Hankel function of the first kind:

$$X^* = \left[ \frac{\beta}{Oh} \right]^{\frac{1}{2}}, \quad \text{and} \quad \mathcal{H}_j^{(1)}(X^*) = \frac{X^* H_{j+1}^{(1)}(X^*)}{H_j^{(1)}(X^*)}. \quad (5.2)$$

For a fixed value of  $Oh$ , we solve iteratively for  $\beta$ . The initial guess used is the solution to the following equation (Prosperetti 1980)

$$\beta^2 - 2Oh[(m+2)(2m+1)]\beta + (m+1)(m-1)(m+2) = 0. \quad (5.3)$$

Once the solution for the first eigenvalue is obtained, we use the associated  $X^*$  for the previous  $Oh$  as the initial guess for the next value of  $Oh$ . We implemented the solution steps in MATLAB and generated the analytical solution for  $0 \leq Oh \leq 1$ .

At steady state, in the absence of gravity and since the liquid surrounding the bubble is stagnant ( $\mathbf{u} = 0$ ), the governing equations reduce to

$$\nabla p = 0, \quad (5.4)$$

and the normal stress boundary condition to

$$-p + P_b = \kappa \text{ on } \Gamma_b. \quad (5.5)$$

Equation (5.4) implies that pressure field in the liquid phase surrounding the bubble is a constant,  $P_a$ , so that the bubble pressure becomes

$$P_b = \kappa + P_a \quad \text{on } \Gamma_b. \quad (5.6)$$

For the linear stability analysis, the value of  $P_a$  was set to zero without loss of generality.

We solve the modified forms of the perturbation equations (4.20)-(4.24) using the base state solutions computed as set out above. Figures 2a and 2b respectively show excellent agreement between the real and imaginary parts of the eigenvalues computed and the analytical solution of (5.1) as a function of the Ohnesorge number for four different azimuthal wavenumbers.

## 6. Additional results: stagnant liquids

Here, we provide additional information associated with the flow fields in the other principal regions around the Taylor bubbles in stagnant liquids, characterised by  $U_m = 0$ .

### 6.1. The film region

The features that define the hydrodynamics of the film region are the stabilisation length  $L_f$ , the equilibrium film thickness  $\Delta_f$ , and the velocity profiles in the fully-developed film. The first two features are crucial parameters as it is expected

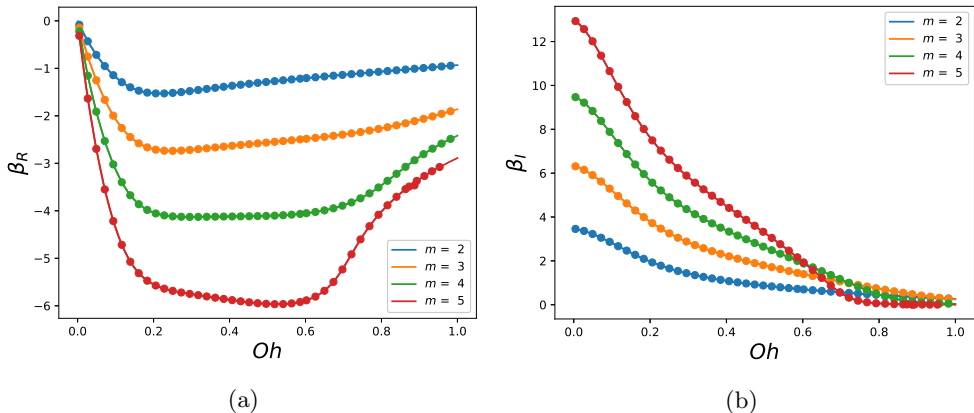


Figure 2: Validation of the theoretical and numerical procedure for an oscillating bubble in the absence of gravitational and boundary effects. Comparison between the amplification rates, (a), and oscillation frequencies, (b), from the analytical solution given by (5.1) (coloured continuous solid line) and our numerically-generated growth rates (coloured markers), for modes  $m = 2, 3, 4$  and  $5$ .

that the flow pattern in the wake of a Taylor bubble becomes independent of the bubble length for bubbles of lengths greater than  $L_f$  and heavily-dependent on  $\Delta_f$  (Nogueira *et al.* 2006). The stabilisation length  $L_f$  is determined to be the point at which the radial velocity component, and the rate of change in the axial velocity component along the interface are less than 1% of their maximum interfacial values. Figure 3a shows that  $L_f$  increases steeply with  $EO$  before plateauing at high  $EO$  for all values of  $N_f$  studied. For a fixed  $EO$  value,  $L_f$  increases with  $N_f$  indicating that the film needs to travel a longer distance below the bubble nose before it becomes fully-developed. However, unlike the dependence on  $N_f$  of the bubble rise speed, or the nose stabilisation length,  $L_f$  does not appear to saturate with increasing  $N_f$ . The results, therefore, indicate that as the viscosity is decreased, it becomes increasingly difficult to obtain a truly fully-developed film around Taylor bubbles that are not extremely long. Below the developing length in the film region, the liquid film is deemed to have attained equilibrium, and the thickness is from there onward constant until the Taylor bubble tail region is approached. The film thickness at the point where the equilibrium film thickness is first attained is measured from our numerical predictions and the result is compared with the theoretical prediction of Brown (1965). From Brown (1965), the equation that relates the equilibrium film thickness to the bubble rise speed, in dimensionless form, can be written as

$$\frac{4N_f}{3U_b}\Delta_f^3 + 2\Delta_f - 1 = 0. \quad (6.1)$$

Using (6.1) together with the expression for  $U_b$

$$U_b = \frac{0.34 \left[ 1 + (14.793/EO)^{3.06} \right]^{-0.58}}{\left[ 1 + \left( N_f \left[ 31.08 \left( 1 + (29.868/EO)^{1.96} \right)^{0.49} \right]^{-1} \right)^\Theta \right]^{-1.0295\Theta^{-1}}} \quad (6.2)$$

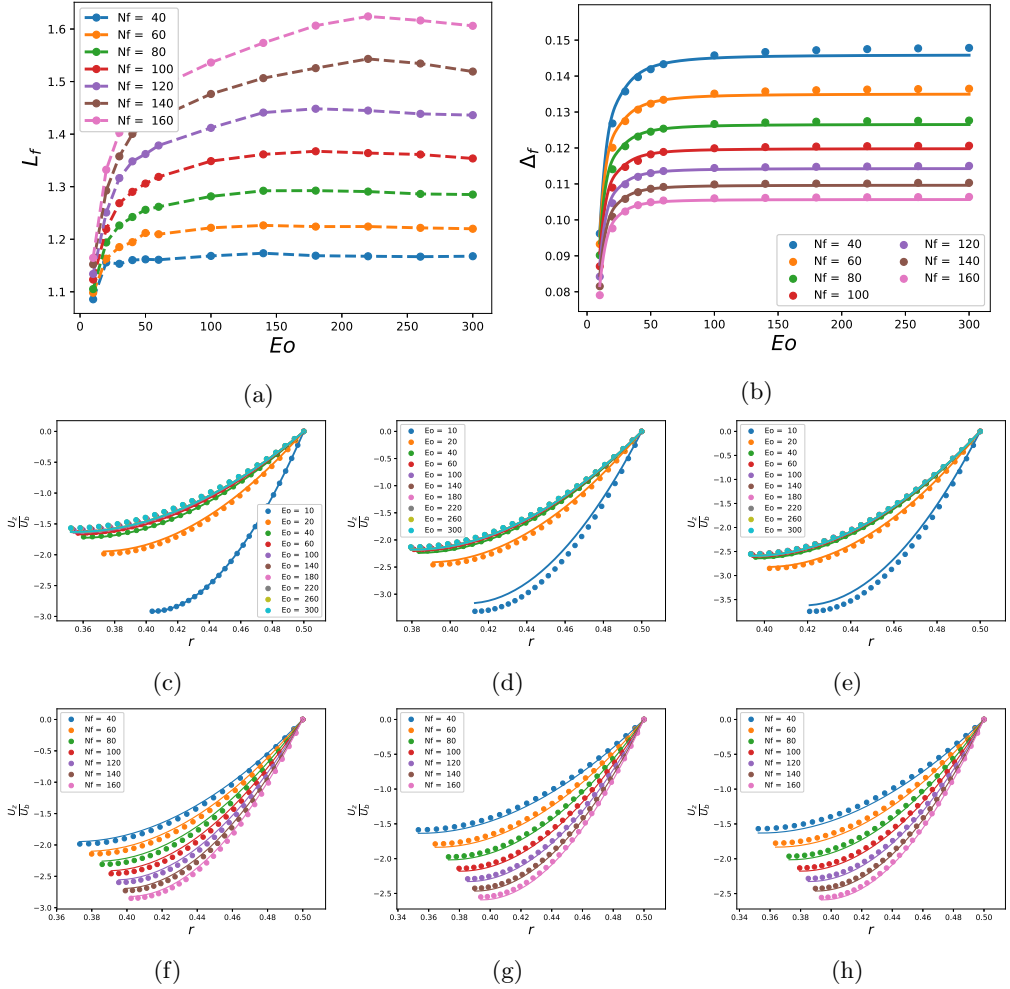


Figure 3: Flow characteristics associated with the film region for bubbles rising in stagnant liquids: stabilisation length  $L_f$  and equilibrium film thickness  $\Delta_f$ , depicted in (a) and (b), respectively, showing a comparison between numerical simulations (coloured markers) and theoretical prediction using (6.1) and (6.2) (coloured continuous solid line) for different  $N_f$  and  $Eo$ ; effect of  $Eo$  on the axial velocity in the fully-developed film region  $u_z$  normalized by  $U_b$  with  $N_f = 40, 100, 160$  shown in (c)-(e), respectively; effect of  $N_f$  on  $u_z/U_b$  with  $Eo = 20, 140, 260$  shown in (f)-(h). In (c)-(h), the numerical simulations are represented by the coloured markers and the theoretical predictions of (6.4) by coloured solid lines.

where the parameter  $\Theta$  is expressed by

$$\Theta = -1.45 \left[ 1 + (24.867 Eo)^{9.93} \right]^{0.094},$$

$\Delta_f$  is computed for different  $N_f$  and  $Eo$ , and the results are compared with our numerical prediction in figure 3b. The numerical and theoretical predictions are in good agreement particularly at higher  $N_f$ , as expected, since the thin liquid film assumption becomes more valid with increasing inverse viscosity number. The decline in the equilibrium film

thickness with  $N_f$  is due to the decrease in the magnitude of the normal stress exerted on the interface as the fluid viscosity is decreased. It is noteworthy that despite the apparent dependence of  $L_f$  on  $EO$  with increasing  $N_f$ ,  $\Delta_f$  remains almost constant beyond  $EO = 100$ .

In order to obtain an approximation of the axial velocity component in the fully-developed film,  $u_z$ , the following reduced version of the dimensionless form of the axial momentum equation in this region is considered (Brown 1965):

$$\frac{1}{r} \frac{d}{dr} \left[ r \frac{du_z}{dr} \right] = -N_f; \quad (6.3)$$

the solution of (6.3) is expressed by

$$u_z = -N_f \left[ \left( \frac{0.25 - r^2}{4} \right) - \frac{1}{2} (0.5 - \Delta_f)^2 \ln \left( \frac{0.5}{r} \right) \right]. \quad (6.4)$$

The predictions from (6.4), scaled using the bubble rise speed and compared to our numerical results are shown in figures 3c-3e and 3f-3h, which highlight the effect of  $N_f$  and  $EO$  on  $u_z/U_b$ , respectively. The improvement in the agreement between the numerical results and the theoretical predictions is noticeable with increasing  $EO$  particularly at high  $N_f$ .

## 6.2. Hydrodynamic features at the wall and interface

### 6.2.1. Wall shear stress

From equation the tangential stress interface condition, the shear stress at any boundary is defined as

$$\boldsymbol{\tau} = \mathbf{n} \cdot \mathbf{T} \times \mathbf{n}. \quad (6.5)$$

For an axisymmetric boundary, the nonzero component of (6.5) simplifies to

$$\tau = N_f^{-1} \left[ \mathbf{n} \cdot \frac{d\mathbf{u}}{ds} + \mathbf{t} \cdot \frac{d\mathbf{u}}{dn} \right], \quad (6.6)$$

which when evaluated at the wall, gives

$$\tau_w = -N_f^{-1} \frac{du_z}{dr}, \quad (6.7)$$

where  $\tau_w$  denotes the dimensionless wall shear stress. In the fully-developed film region, using (6.4),  $\tau_w$  reads

$$\tau_w = 0.25 - (0.5 - \Delta_f)^2, \quad (6.8)$$

which is a constant whose dependence on  $N_f$  and  $EO$  enters (6.8) through the variation of  $\Delta_f$  with these parameters via (6.2) and (6.1). A comparison of the predictions of equation with the numerically computed results for  $\tau_w$  using (6.7) is shown in figures (4a)-(4f). Beyond the limit at which  $EO$  exerts a strong influence on the dynamics of the bubble, i.e., for  $EO \gtrsim 100$ , (6.8) adequately predicts the effect of  $N_f$  and  $EO$  on  $\tau_w$  in the developed film region. While an increase in  $N_f$  leads to a reduction in  $\tau_w$ ,  $EO$  has no significant impact on it beyond  $EO \sim 100$ . Both effects can be related to that of the parameters on the equilibrium film thickness and its velocity profiles, shown in figures 3b, (3c)-(3e), and (3f)-(3h), respectively. The apparent peaks observed in figures (4a)-(4c) and (4d)-(4f) when surface tension effects are strong for small  $EO$  can be related to the undulation that appears towards the end of the liquid film, with the influence becoming more pronounced as  $N_f$  is increased and  $EO$  decreased. Lastly, the maximum wall shear stress,  $\tau_w^m$ , for the combined effect of  $N_f$  and  $EO$ , is plotted in figure 4g.

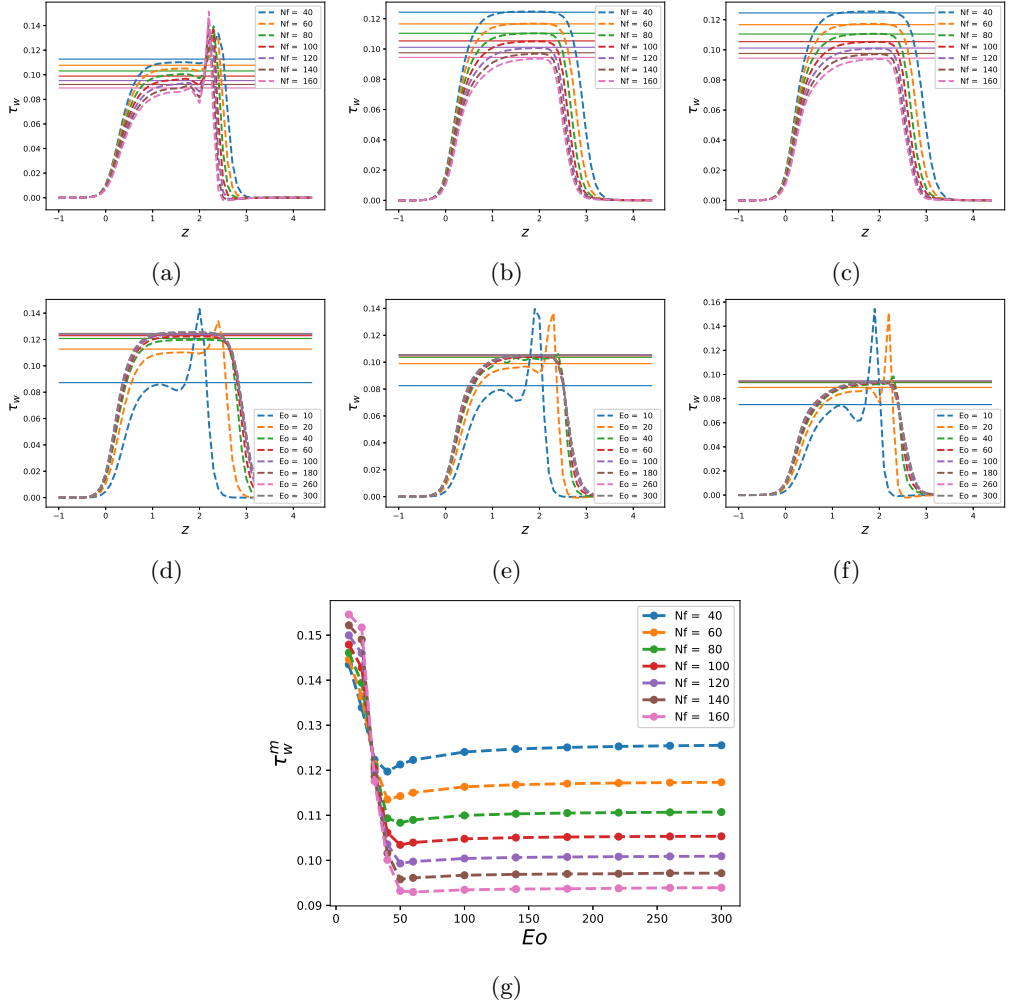


Figure 4: Shear stress at the wall boundary: effect of  $N_f$  with  $E_o = 20, 140, 260$  shown in (a)-(c), respectively; effect of  $E_o$  with  $N_f = 40, 100, 160$  shown in (d)-(f), respectively; (g) effects of  $N_f$  and  $E_o$  on the maximum wall shear stress. In (a)-(f), our numerical results are shown using broken lines and the predictions of (6.8) in the fully-developed film region using solid lines.

### 6.2.2. Interface normal stress

From the normal stress interface condition, the normal stress at the interface in the direction of unit normal to the interface is defined as

$$\sigma_n = -\mathbf{n} \cdot \mathbf{T} \cdot \mathbf{n} = - \left[ -p + 2N_f^{-1} \mathbf{n} \cdot \frac{d\mathbf{u}}{dn} \right]. \quad (6.9)$$

Expressing the normal stress in terms of the total pressure by adding the gravity term to the hydrodynamic pressure, the normal stress interface condition becomes

$$\sigma_n^* = - \left[ -p_T + 2N_f^{-1} \mathbf{n} \cdot \frac{d\mathbf{u}}{dn} \right] = P_b - E_o^{-1} \kappa, \quad (6.10)$$

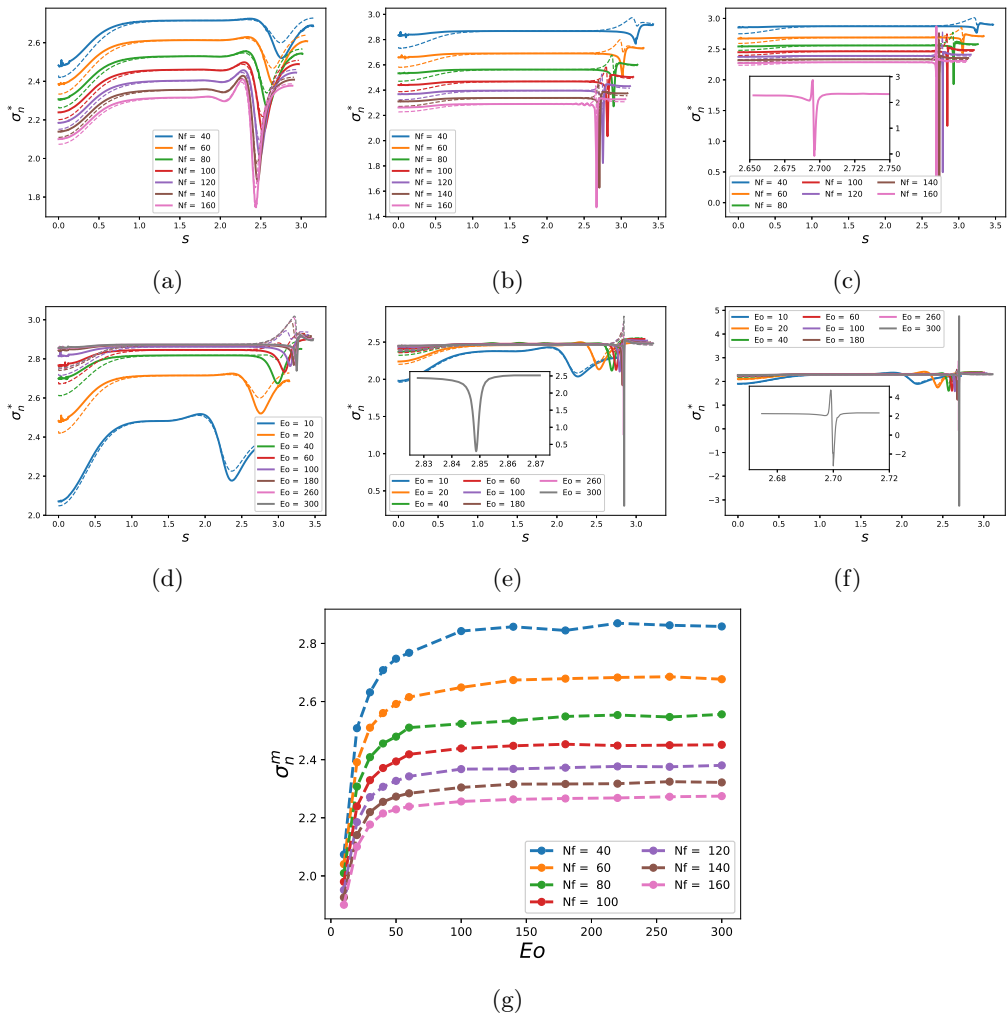


Figure 5: Normal stress (solid lines) and total pressure (broken lines) at the interface: effect of  $N_f$  with  $Eo = 20, 140, 260$  shown in (a)-(c), respectively; effect of  $Eo$  with  $N_f = 40, 100, 160$  shown in (d)-(f), respectively; (g) effects of  $N_f$  and  $Eo$  on the maximum interface normal stress. Panels (c), (e), and (f) show an enlarged view of the curves for  $N_f = 160$ ,  $Eo = 300$ , and  $Eo = 300$ , respectively, for  $2.5 \leq s \leq 3$ .

where  $p_T = p + z$ . figures (5a)-(5c) and (5d)-(5f) show the effects of  $N_f$  and  $Eo$  on the interface normal stress and total pressure. It is apparent that the normal stress decreases with  $N_f$  and it becomes weakly-dependent on  $Eo$  for  $Eo \gtrsim 100$ . In the fully-developed liquid film region, both the pressure and the normal stress match in order to satisfy (6.10). This is because in this region, the interface has approximately zero curvature, and  $u_r = du_r/dn = 0$ , making the viscous stress and the stress due to curvature in the  $r - z$  plane contributions zero. Thus, (6.10) reduces to  $\sigma_n^* = p_T = P_b - Eo^{-1}\kappa_b \approx P_b$ . Since the bubble pressure is a constant, the implication of this is that the viscous and curvature forces are only important in the nose and bottom of the bubble and it is the interplay between them that determines the shape of these regions. For the observed sharp peaks in the interface normal stress around the bubble bottom, particularly for

higher  $Eo$  and  $N_f$  such as the ones shown in figures 5c, 5e, and 5f, it is clear from figures 6a-6d, the insets shown in these figures that the bubble bottom and the tail regions are well resolved. In figure 5g, the maximum normal stress,  $\sigma_n^m$  exerted on the interface was extracted to highlight its dependence on  $N_f$  and  $Eo$ .

### 6.3. Hydrodynamic features of bottom region

The features in this region encompass those that define the bottom of the bubble which are the shape of the bottom and the length of the developing length below the bottom, and those that define the wake, if present, which are the length of the wake and the position vector of the vortex eye. We focus here on the shape of the bottom which is determined from the bottom curvature.

The effects of varying flow conditions on the Taylor bubble bottom shape are quantitatively examined using the sign of the radius of curvature. Because of the varying shapes that are associated with bubble bottom, it is more convenient and sufficient to define the shape of the bubble bottom based on the curvature evaluated at the bottom along the axis of symmetry. Essentially, a positive (negative) radius of curvature signifies a convex (concave) bottom shape with respect to the liquid phase. figure 6e shows the mean radius of curvature  $R_b$  for different  $N_f$  and varying  $Eo$ . It is clear that  $R_b$  becomes independent of  $Eo$  for  $Eo \gtrsim 100$ . For  $Eo < 100$ , it is seen that  $R_b$  exhibits a non-monotonic dependence on  $Eo$  which becomes particularly pronounced for increasing  $N_f$ . The behaviour depicted in figure 6e is reflected in the shape of the bubble bottom and its dependence on  $Eo$  and  $N_f$  as illustrated in figures 6f and 6g, respectively. Inspection of these figures reveals that with increasing  $N_f$  and  $Eo$  the bubble tail becomes more pointed. It is possible that for larger values of  $N_f$  and  $Eo$  a skirted bubble may form followed by the eventual breakup of the protruding tail structure into smaller bubbles.

## 7. Additional results: upward liquid flow

Here, we provide results associated with the case of Taylor bubble motion in upward liquid flows, characterised by  $U_m > 0$ . In figure 7a, the numerical simulation results for upward liquid flow are compared with predictions based on the correlation of Nicklin *et al.* (1962) given by

$$U_b = C_1 \bar{U}_L + C_0, \quad (7.1)$$

with expressions for  $C_0$  and  $C_1$  provided by Bendiksen (1985) taking into consideration the effect of  $Eo$  as

$$C_0 = \frac{0.486}{\sqrt{2}} \sqrt{1 + 20 \left(1 - \frac{6.8}{Eo}\right) \left\{ \frac{1 - 0.96e^{-0.0165Eo}}{1 - 0.52e^{-0.0165Eo}} \right\}}, \quad (7.2)$$

$$C_1 = 1.145 \left[ 1 - \frac{20}{Eo} (1 - e^{-0.0125Eo}) \right]. \quad (7.3)$$

It is evident that (7.1) with (7.2) and (7.3) over-predict the bubble rise speed. This is because the expressions for  $C_0$  and  $C_1$  were derived for cases in which flow due to the bubble motion was considered to be inviscid, an assumption that gains with increasing  $N_f$ . The agreement with the numerical results improves significantly when the correlation of Viana *et al.* (2003) is used to calculate  $C_0$ ; this correlation accounts for the effects of viscosity and surface tension and the agreement improves further with increasing  $N_f$ . We can estimate values for  $C_0$  and  $C_1$  from our numerical simulations for various  $N_f$  and

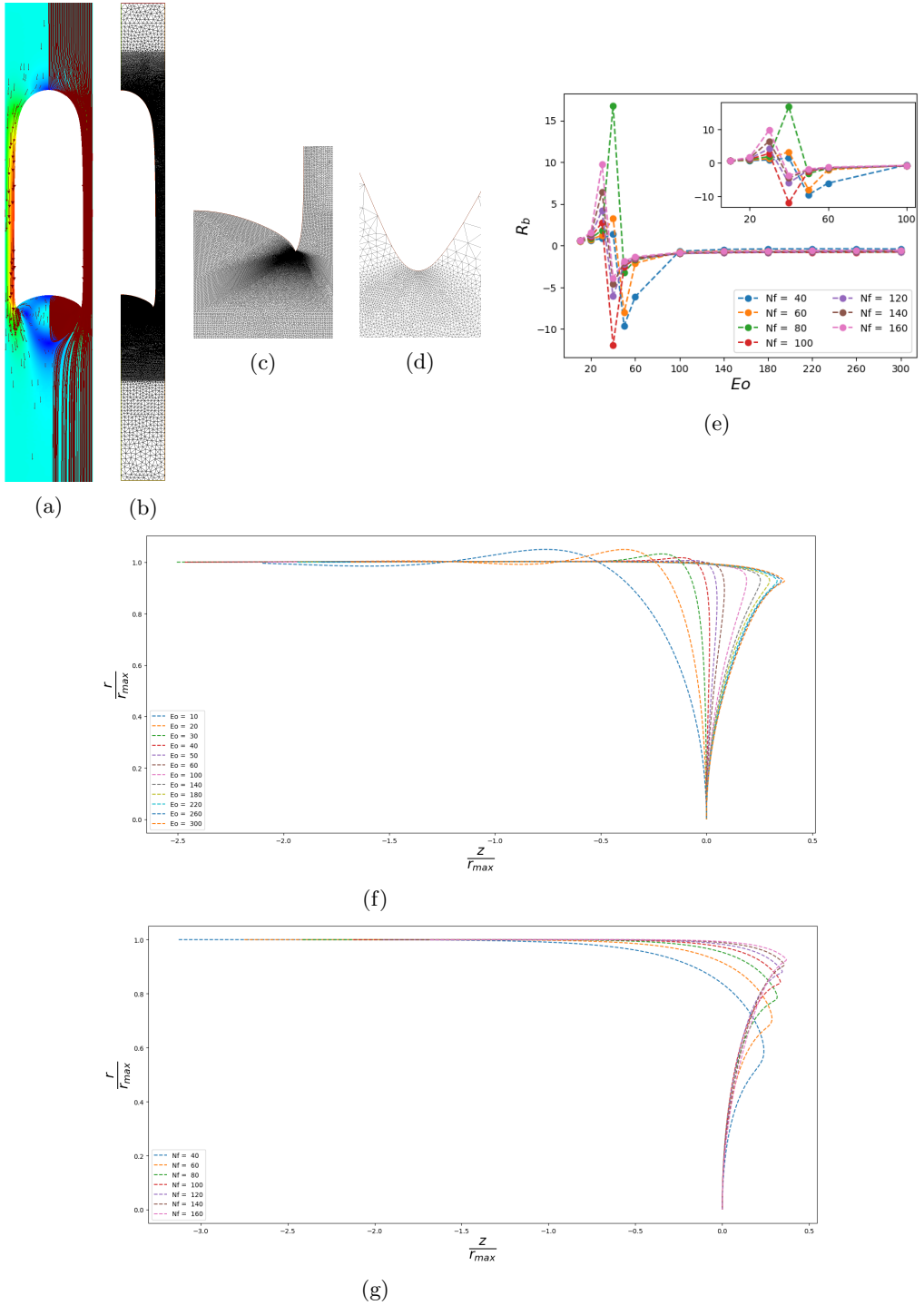


Figure 6: Flow characteristics of the bottom region for a bubble rising in a stagnant liquid: shape, (a), and mesh structure, (b), for  $N_f = 160$  and  $E_o = 300$ ; enlarged views of the bottom, (c), and tail tip mesh structures, (d); (e) influence of  $N_f$  and  $E_o$  on the Taylor bubble bottom radius of curvature  $R_b$ ; bottom deformation: influence of  $E_o$  with  $N_f = 160$ , (f), and influence of  $N_f$  for  $E_o = 300$ , (g).

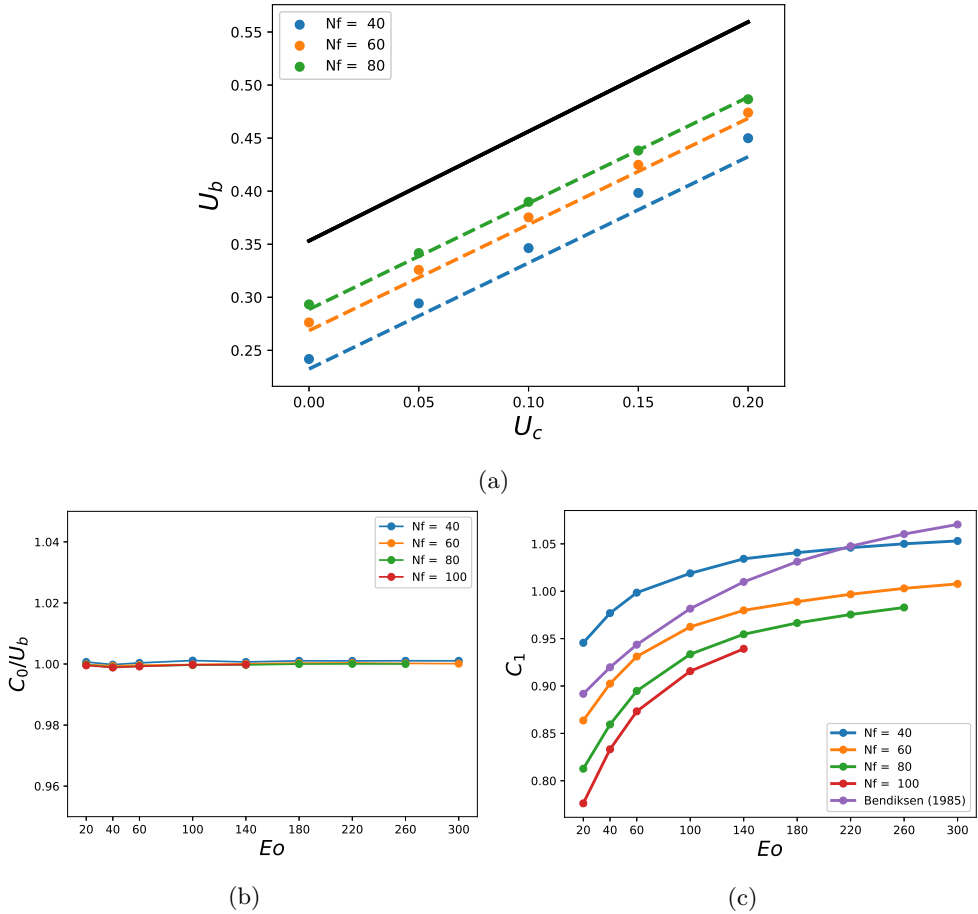


Figure 7: Effect of imposed upward liquid flow speed  $U_m$  on the bubble rise speed  $U_b$  for varying  $N_f$ , (a): comparison between the numerical results (coloured markers), predictions based on the Nicklin *et al.* (1962) correlation (7.1) (black solid line) with the Bendiksen (1985) relations (7.2) and (7.3) used for coefficients  $C_0$  and  $C_1$ , and predictions using the Viana *et al.* (2003) correlation for  $C_0$  given by (6.2) and the Bendiksen (1985) relation for  $C_1$  expressed by (7.3) (coloured dashed lines); effect of  $N_f$  and  $Eo$  on the numerically-generated  $C_0$  (normalised by  $U_b$ ), (b), and  $C_1$ , (c).

$Eo$ , and the results are shown in figures 7b and 7c, respectively. It is seen that  $C_0/U_b$  remains approximately equal to unity over the range of  $N_f$  and  $Eo$  studied, while  $C_1$  increases monotonically with  $Eo$  for all  $N_f$  considered reaching a plateau at high  $Eo$ .

## 8. Energy balance formulation

### 8.1. Energy equation

We derive energy equation from the derived normal mode perturbation equations for the velocity components, (4.20)-(4.22), by setting the test functions for the latter to equal the complex conjugate of the velocity perturbations,  $\bar{\Phi}_r = \hat{u}_r^*$ ,  $\bar{\Phi}_\theta = \hat{u}_\theta^*$ ,  $\bar{\Phi}_z = \hat{u}_z^*$ , followed

by necessary simplifications:

$$\begin{aligned}
& \beta_R \int_{\Omega^0} \left\{ |\hat{u}_r|^2 + |\hat{u}_\theta|^2 + |\hat{u}_z|^2 \right\} d\Omega^0 + \int_{\Omega^0} \left\{ |\hat{u}_r|^2 \frac{\partial u_r^0}{\partial r^0} + |\hat{u}_z|^2 \frac{\partial u_z^0}{\partial z} + \frac{|\hat{u}_\theta|^2 u_r^0}{r} \right. \\
& + \left. \left( \frac{\partial u_r^0}{\partial z} + \frac{\partial u_z^0}{\partial r^0} \right) \Re \{ \hat{u}_r \hat{u}_z^* \} \right\} d\Omega^0 + \int_{\Omega} N_f^{-1} \left\{ 2 \left| \frac{\partial \hat{u}_r}{\partial r} \right|^2 + 2 \left| \frac{\partial \hat{u}_z}{\partial z} \right|^2 \right. \\
& + \frac{1}{r^2} \left[ (2 + m^2) |\hat{u}_r|^2 + (1 + 2m^2) |\hat{u}_\theta|^2 + m^2 |\hat{u}_z|^2 \right] + \left| \frac{\partial \hat{u}_\theta}{\partial r} \right|^2 + \left| \frac{\partial \hat{u}_\theta}{\partial z} \right|^2 \\
& + \left| \frac{\partial \hat{u}_r}{\partial z} + \frac{\partial \hat{u}_z}{\partial r} \right|^2 - \frac{1}{r} \frac{\partial |\hat{u}_\theta|^2}{\partial r} + \frac{6m}{r^2} \Im m \{ \hat{u}_r \hat{u}_\theta^* \} + \frac{2m}{r} \Im m \left( \hat{u}_z^* \frac{\partial \hat{u}_\theta}{\partial z} + \hat{u}_r^* \frac{\partial \hat{u}_\theta}{\partial r} \right) \left. \right\} d\Omega^0 \\
& - \int_{\Gamma_b^0} Eo^{-1} \left\{ -\frac{d\hat{h}}{ds} \left[ \mathbf{n} \cdot \frac{d\hat{\mathbf{u}}^*}{ds} - \kappa_a (\mathbf{t} \cdot \hat{\mathbf{u}}^*) \right] + \hat{h} \left[ \kappa_a^2 + \kappa_b^2 - \frac{m^2}{r^2} \right] \mathbf{n} \cdot \hat{\mathbf{u}}^* \right\} d\Gamma_b^0 \\
& - \int_{\Gamma_b^0} \left\{ \hat{h} n_z (\mathbf{n} \cdot \hat{\mathbf{u}}^*) \right\} d\Gamma_b^0 \\
& + \int_{\Gamma_b^0} \hat{h} \left\{ (\mathbf{u}^0 \cdot \mathbf{t}) \left[ \frac{d\mathbf{u}^0}{ds} \cdot \hat{\mathbf{u}}^* \right] + \left[ -p^0 + 2N_f^{-1} \left( \mathbf{t} \cdot \frac{d\mathbf{u}^0}{ds} \right) \right] (\mathbf{t} \cdot \frac{d\hat{\mathbf{u}}^*}{ds}) \right. \\
& + \left. \left[ -p^0 + 2N_f^{-1} \frac{u_r^0}{r} \right] \left( \frac{\hat{u}_r^*}{r} - im \frac{\hat{u}_\theta^*}{r} \right) \right\} d\Gamma_b^0 \\
& + \int_{\Gamma_b^0} \left\{ \left[ Eo^{-1} \kappa + z - P_b^0 \right] \left[ (\mathbf{t} \cdot \hat{\mathbf{u}}^*) \frac{d\hat{h}}{ds} + \hat{h} \left( im \frac{\hat{u}_\theta^*}{r} \right) + \hat{h} \kappa (\mathbf{n} \cdot \hat{\mathbf{u}}^*) \right] \right\} d\Gamma_b^0 = 0 \quad (8.1)
\end{aligned}$$

where the symbol  $|\cdot|$  represents the magnitude of a complex function;  $\Re$  and  $\Im$  denote the real and imaginary part of a complex function, respectively. Equation (8.1) is the energy budget formulation that governs the evolution of the disturbance kinetic equation which following Boomkamp & Miesen (1996), can be expressed as

$$\dot{E} = REY + DIS + INT, \quad (8.2)$$

where  $\dot{E}$  corresponds to the time range of change of the perturbation kinetic energy given by the following relation

$$\dot{E} = \beta_R \int_{\Omega^0} \left\{ |\hat{u}_r|^2 + |\hat{u}_\theta|^2 + |\hat{u}_z|^2 \right\} d\Omega^0 \equiv \beta_R KIN, \quad (8.3)$$

wherein  $KIN$  represents the total kinetic energy associated with the perturbation velocity field, which equals  $\dot{E}$  when multiplied by the growth rate  $\beta_R$  (which is positive for an unstable flow). We also introduce the following definitions for the terms  $REY$  and  $DIS$  that appear on the right-hand-side of (8.2) (Boomkamp & Miesen 1996):

$$REY = - \int_{\Omega^0} \left\{ |\hat{u}_r|^2 \frac{\partial u_r^0}{\partial r^0} + |\hat{u}_z|^2 \frac{\partial u_z^0}{\partial z} + \frac{|\hat{u}_\theta|^2 u_r^0}{r} + \left( \frac{\partial u_r^0}{\partial z} + \frac{\partial u_z^0}{\partial r^0} \right) \Re \{ \hat{u}_r \hat{u}_z^* \} \right\} d\Omega^0, \quad (8.4)$$

$$\begin{aligned}
DIS = & - \int_{\Omega} N_f^{-1} \left\{ 2 \left| \frac{\partial \hat{u}_r}{\partial r} \right|^2 + 2 \left| \frac{\partial \hat{u}_z}{\partial z} \right|^2 + \frac{1}{r^2} \left[ (2 + m^2) |\hat{u}_r|^2 + (1 + 2m^2) |\hat{u}_\theta|^2 \right. \right. \\
& + m^2 |\hat{u}_z|^2 \left. \left. + \left| \frac{\partial \hat{u}_\theta}{\partial r} \right|^2 + \left| \frac{\partial \hat{u}_\theta}{\partial z} \right|^2 + \left| \frac{\partial \hat{u}_r}{\partial z} + \frac{\partial \hat{u}_z}{\partial r} \right|^2 - \frac{1}{r} \frac{\partial |\hat{u}_\theta|^2}{\partial r} + \frac{6m}{r^2} \Im m \{ \hat{u}_r \hat{u}_\theta^* \} \right. \right. \\
& \left. \left. + \frac{2m}{r} \Im m \left( \hat{u}_z^* \frac{\partial \hat{u}_\theta}{\partial z} + \hat{u}_r^* \frac{\partial \hat{u}_\theta}{\partial r} \right) \right\} d\Omega. \tag{8.5}
\end{aligned}$$

Here, *REY* denotes the rate of energy transfer by the ‘‘Reynolds stress’’ (product of two perturbations analogues to the turbulent Reynolds stress) from the base flow to the disturbed flow, and *DIS* represents the rate of viscous dissipation of energy of the disturbed flow. We also provide a breakdown for *INT*, the rate of work done by the velocity and stress disturbances in deforming the interface (Boomkamp & Miesen 1996) which we have decomposed into its normal, *NOR*, and tangential, *TAN*, components with *NOR* further subdivided into *TEN*, *HYD*, and *BUB*, representing work done at the interface against surface tension, gravity, and bubble pressure, respectively.

$$INT = NOR + TAN, \tag{8.6a}$$

$$NOR = TEN + HYD + BUB, \tag{8.6b}$$

Expressions for *TAN*, *NOR*, and *TEN*, *HYD* and *BUB*, are respectively provided by

$$\begin{aligned}
TAN = & \mathbb{R} \left\{ - \int_{\Gamma_b^0} \hat{h} \left\{ (\mathbf{u}^0 \cdot \mathbf{t}) \left[ \frac{d\mathbf{u}^0}{ds} \cdot \hat{\mathbf{u}}^* \right] + \left[ -p^0 + 2N_f^{-1} \left( \mathbf{t} \cdot \frac{d\mathbf{u}^0}{ds} \right) \right] \left( \mathbf{t} \cdot \frac{d\hat{\mathbf{u}}^*}{ds} \right) \right. \right. \\
& + \left. \left[ -p^0 + 2N_f^{-1} \frac{u_r^0}{r} \right] \left( \frac{\hat{u}_r^*}{r} - im \frac{\hat{u}_\theta^*}{r} \right) \right\} d\Gamma_b^0 + \int_{\Gamma_b^0} Eo^{-1} \left\{ \frac{d\hat{h}}{ds} [\kappa_a (\mathbf{t} \cdot \hat{\mathbf{u}}^*)] \right\} d\Gamma_b^0 \\
& - \int_{\Gamma_b^0} \left\{ [Eo^{-1} \kappa + z - P_b^0] \left[ (\mathbf{t} \cdot \hat{\mathbf{u}}^*) \frac{d\hat{h}}{ds} + \hat{h} \left( im \frac{\hat{u}_\theta^*}{r} \right) \right] \right\} d\Gamma_b^0 \left. \right\}, \tag{8.7}
\end{aligned}$$

$$\begin{aligned}
NOR = & \mathbb{R} \left\{ \int_{\Gamma_b^0} Eo^{-1} \left\{ - \frac{d\hat{h}}{ds} \left[ \mathbf{n} \cdot \frac{d\hat{\mathbf{u}}^*}{ds} \right] + \hat{h} \left[ \kappa_a^2 + \kappa_b^2 - \frac{m^2}{r^2} \right] \mathbf{n} \cdot \hat{\mathbf{u}}^* \right\} d\Gamma_b^0 \right. \\
& \left. + \int_{\Gamma_b^0} \left\{ \hat{h} n_z (\mathbf{n} \cdot \hat{\mathbf{u}}^*) \right\} d\Gamma_b^0 - \int_{\Gamma_b^0} \left\{ [Eo^{-1} \kappa + z - P_b^0] \left[ \hat{h} \kappa (\mathbf{n} \cdot \hat{\mathbf{u}}^*) \right] \right\} d\Gamma_b^0 \right\}, \tag{8.8}
\end{aligned}$$

$$TEN = \mathbb{R} \left\{ \int_{\Gamma_b^0} Eo^{-1} \left\{ - \frac{d\hat{h}}{ds} \left[ \mathbf{n} \cdot \frac{d\hat{\mathbf{u}}^*}{ds} \right] + \hat{h} \left[ \kappa_a^2 + \kappa_b^2 - \kappa^2 - \frac{m^2}{r^2} \right] \mathbf{n} \cdot \hat{\mathbf{u}}^* \right\} d\Gamma_b^0 \right\}, \tag{8.9}$$

$$HYD = \mathbb{R} \left\{ \int_{\Gamma_b^0} \left\{ \hat{h} (n_z - z\kappa) (\mathbf{n} \cdot \hat{\mathbf{u}}^*) \right\} d\Gamma_b^0 \right\}, \tag{8.10}$$

$$BUB = \mathbb{R} \left\{ \int_{\Gamma_b^0} \left\{ P_b^0 \left[ \hat{h} \kappa (\mathbf{n} \cdot \hat{\mathbf{u}}^*) \right] \right\} d\Gamma_b^0 \right\}. \tag{8.11}$$

Furthermore, it is instructive to split  $TAN$  into its constituent components based on the base state groups that supply energy to the perturbations as follow:

$$TAN_{ut} = \mathbb{R} \left\{ - \int_{\Gamma_b^0} \hat{h}(\mathbf{u}^0 \cdot \mathbf{t}) \left[ \frac{d\mathbf{u}^0}{ds} \cdot \hat{\mathbf{u}}^* \right] \right\}, \quad (8.12a)$$

$$TAN_{strs} = \mathbb{R} \left\{ - \int_{\Gamma_b^0} \hat{h} \left\{ \left[ -p^0 + 2N_f^{-1} \left( \mathbf{t} \cdot \frac{d\mathbf{u}^0}{ds} \right) \right] \left( \mathbf{t} \cdot \frac{d\hat{\mathbf{u}}^*}{ds} \right) + \left[ -p^0 + 2N_f^{-1} \frac{u_r^0}{r} \right] \left( \frac{\hat{u}_r^*}{r} - im \frac{\hat{u}_\theta^*}{r} \right) \right\} \right\}, \quad (8.12b)$$

$$TAN_{ts} = \mathbb{R} \left\{ \int_{\Gamma_b^0} Eo^{-1} \left\{ \frac{d\hat{h}}{ds} [\kappa_a(\mathbf{t} \cdot \hat{\mathbf{u}}^*)] - \kappa \left[ (\mathbf{t} \cdot \hat{\mathbf{u}}^*) \frac{d\hat{h}}{ds} + \hat{h} \left( im \frac{\hat{u}_\theta^*}{r} \right) \right] \right\} d\Gamma_b^0 \right\}, \quad (8.12c)$$

$$TAN_g = \mathbb{R} \left\{ \int_{\Gamma_b^0} -z \left[ (\mathbf{t} \cdot \hat{\mathbf{u}}^*) \frac{d\hat{h}}{ds} + \hat{h} \left( im \frac{\hat{u}_\theta^*}{r} \right) \right] d\Gamma_b^0 \right\}, \quad (8.12d)$$

$$TAN_{pb} = \mathbb{R} \left\{ \int_{\Gamma_b^0} P_b \left[ (\mathbf{t} \cdot \hat{\mathbf{u}}^*) \frac{d\hat{h}}{ds} + \hat{h} \left( im \frac{\hat{u}_\theta^*}{r} \right) \right] d\Gamma_b^0 \right\}. \quad (8.12e)$$

so that

$$TAN = TAN_{ut} + TAN_{strs} + TAN_{ts} + TAN_g + TAN_{pb} \quad (8.13)$$

The terms  $TAN_{ut}$ ,  $TAN_{strs}$ ,  $TAN_{ts}$ ,  $TAN_g$  and  $TAN_{pb}$  denote the contributions to  $TAN$  due to streaming tangential velocity, tangential stress, surface tension, gravity and bubble pressure on the interface as captured by the base state terms  $\mathbf{u} \cdot \mathbf{t}$ ,  $\left[ -p^0 + 2N_f^{-1} \left( \mathbf{t} \cdot \frac{d\mathbf{u}^0}{ds} \right) \right] + \left[ -p^0 + 2N_f^{-1} \frac{u_r^0}{r} \right]$ ,  $Eo$ ,  $z$  and  $P_b$  in the expressions, respectively. The base state contribution to  $TAN_{strs}$  is related to the tangential stress because it can be obtained by taking the double dot product of the stress tensor and the tangential projection operator,  $(\mathbf{I} - \mathbf{n} \otimes \mathbf{n})$ .

## 8.2. Interface energy reformulation

It is also worth asking what would have happened had the classification of the interface energy terms in our energy equation into  $TAN$  or  $NOR$  been based on whether the base state terms that interact with the disturbances are tangential or normal to the interface (rather than whether the disturbances themselves are tangential or normal to the interface). In that case,  $TAN$  will have only comprised two energy terms ( $TAN_{ut}$  and  $TAN_{strs}$ ); the remaining three would have been moved to  $NOR$  with  $TAN_{ts}$ ,  $TAN_g$  and  $TAN_{pb}$  added to  $TEN$ ,  $HYD$ , and  $BUB$ , respectively. This implies that the normal base state terms (surface tension, gravity and bubble pressure) could interact with the normal or/and tangential disturbance at the interface.

The implication of this re-definition of  $TAN$  and  $NOR$  on the results is shown in figures 1-5 below, with figure 1, 2, 3 & 4 (different  $U_m$ ), and 5 corresponding to figures 22, 23, 24, and 25, in the main paper, respectively. These figures show that the dominant energy term that drives the instability at the onset is  $HYD$  for  $Eo > 20$  and switches  $TAN$  for  $Eo = 20$ . This mirrors the trend in base state curvature radius versus  $Eo$  plot which indicates the existence of a minimum  $Eo$  in the interval  $[20, 30)$ . In addition, for  $Eo > 20$ , it can be observed that as  $U_m$  is increased beyond the critical value of  $U_m$

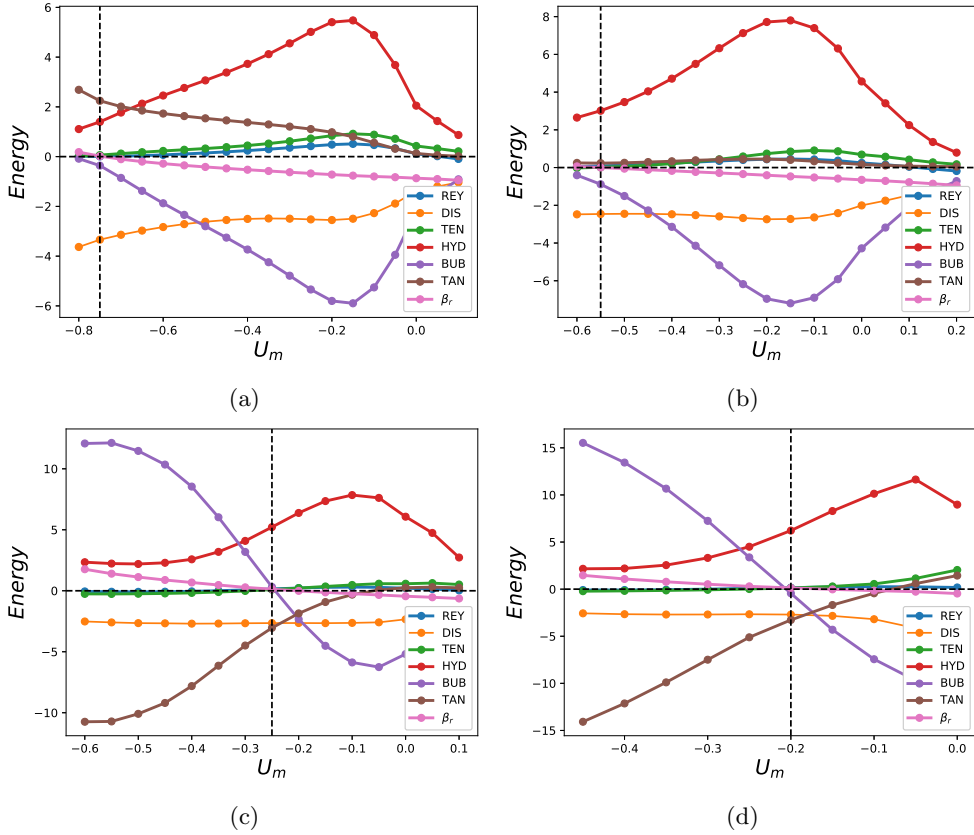


Figure 8: Breakdown of the energy budget for the eigenmode  $m = 1$  as a function of  $U_m$  for  $Eo = 20, 60, 180$ , and  $300$ , shown in (a)-(d), respectively, with  $N_f = 80$ . In each panel, the vertical dashed line marks the  $U_m$  value for which  $\beta_R = 0$ .

(at which the first instability is observed) there exists a limit of  $U_m$  beyond which *BUB* overtakes *HYD* as the dominant energy term.

## REFERENCES

- BENDIKSEN, K. 1985 On the motion of long bubbles in vertical tubes. *Int. J. Multiphase Flow* **11**, 797–812.
- BOOMKAMP, P.A.M. & MIESEN, R.H.M. 1996 Classification of instabilities in parallel two-phase flow. *Int. J. Multiphase Flow* **22**, 67–88.
- BROWN, R.A.S. 1965 The mechanics of large gas bubbles in tubes I. Bubble velocities in stagnant liquids. *Can. J. Chem. Eng* **43**, 217–223.
- BUGG, J. D. & SAAD, G. A. 2002 The velocity field around a Taylor bubble rising in a stagnant viscous fluid: Numerical and experimental results. *Int. J. Multiphase Flow* **28**, 791–803.
- CAIRNCROSS, R.A., SCHUNK, P.R., BAER, T.A., RAO, R.R. & SACKINGER, P.A. 2000 A finite element method for free surface flows of incompressible fluids in three dimensions. Part I. Boundary fitted mesh motion. *Int. J. Numer. Meth. Fluids* **33**, 375–403.
- CARVALHO, M.S. & SCRIVEN, L.E. 1999 Three-dimensional stability analysis of free surface flows: application to forward deformable roll coating. *J. Comput. Phys.* **151**, 534–562.
- CHIREUX, V., FABRE, D., RISSO, F. & TORDJEMAN, P. 2015 Oscillations of a liquid bridge resulting from the coalescence of two droplets. *Physics of Fluids* **27**, 062103.

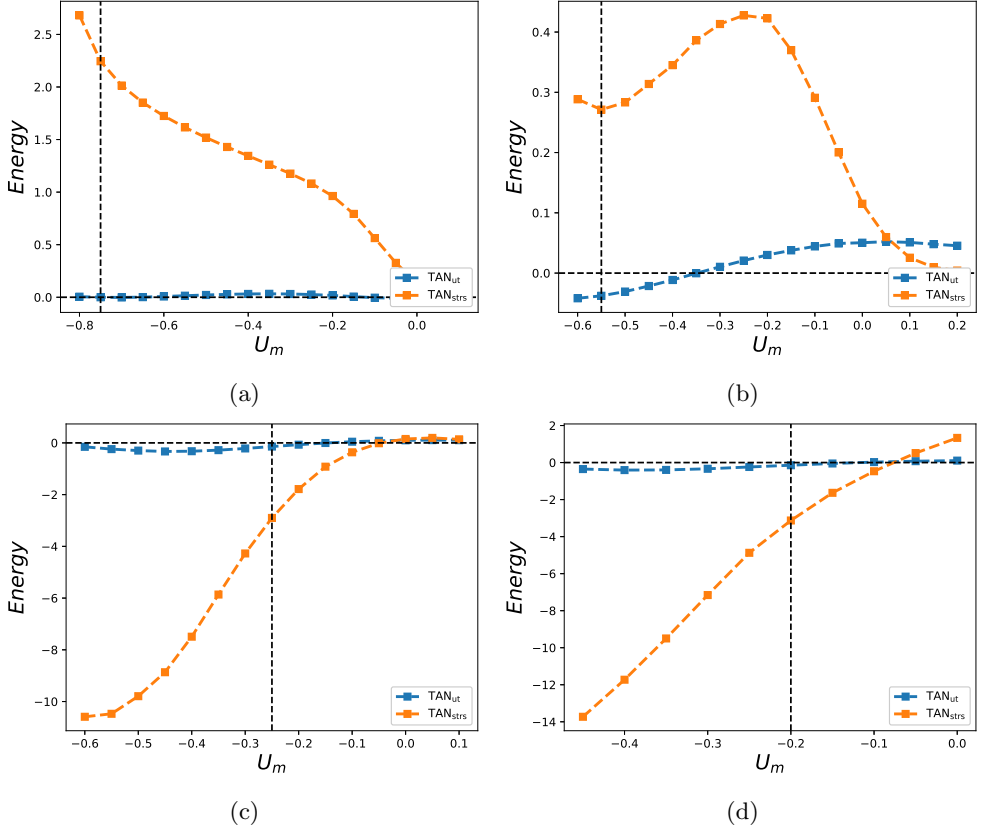


Figure 9: Breakdown of  $TAN$  for the eigenmode  $m = 1$  into its constituent components as a function of  $U_m$  for  $E_o = 20, 60, 180,$  and  $300$ , shown in (a)-(d), respectively, with  $N_f = 80$ . In each panel, the vertical dashed line marks the  $U_m$  value for which  $\beta_R = 0$ .

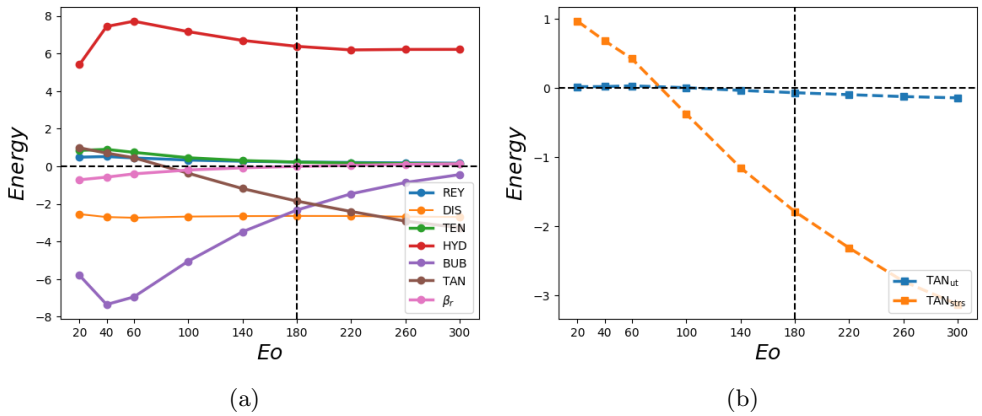


Figure 10: Breakdown of the energy budget, (a), and the  $TAN$  constituents, (b), with  $E_o$ , for  $m = 1$  with  $N_f = 80$  and  $U_m = -0.20$ . The vertical dashed line marks the  $E_o$  value for which  $\beta_R = 0$ .

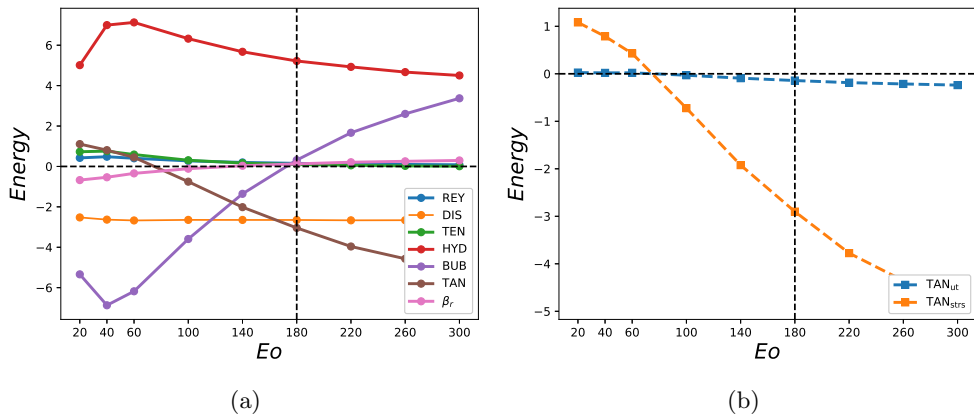


Figure 11: Breakdown of the energy budget, (a), and the  $TAN$  constituents, (b), with  $Eo$ , for  $m = 1$  with  $N_f = 80$  and  $U_m = -0.25$ . The vertical dashed line marks the  $Eo$  value for which  $\beta_R = 0$ .

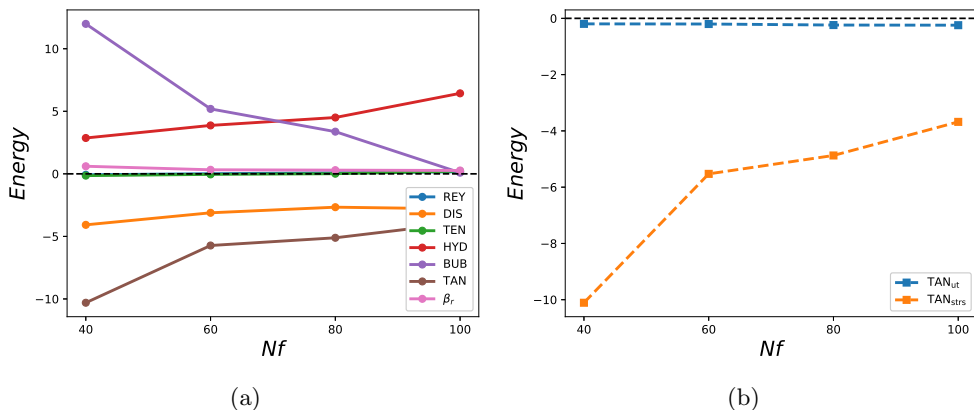


Figure 12: Breakdown of the energy budget, (a), and  $TAN$  constituents, (b), with  $N_f$ , for  $m = 1$  with  $Eo = 300$  and  $U_m = -0.25$ .

HEINRICH, J.C. & PEPPER, D.W. 1999 *Intermediate finite element method : fluid flow and heat transfer applications*. Taylor & Francis Group.

KRUYT, N.P., CUVELIER, C., SEGAL, A. & VAN DER ZANDEN, J. 1988 A total linearization method for solving viscous free boundary flow problems by the finite-element method. *Int. J. Numer. Methods Fluids* **8**, 351–363.

MILLER, C.A. & SCRIVEN, L.E. 1968 The oscillations of a fluid droplet immersed in another fluid. *J. Fluid Mech.* **32**, 417–435.

NICKLIN, D., WILKES, J. & DAVIDSON, J. 1962 Two-phase flow in vertical tubes. *Trans. Inst. Chem. Engrs* **40**, 61–68.

NOGUEIRA, S., RIETHMULLER, M.L., CAMPOS, J.B.L.M. & PINTO, A.M.F.R. 2006 Flow patterns in the wake of a Taylor bubble rising through vertical columns of stagnant and flowing Newtonian liquids: an experimental study. *Chem. Eng. Sci.* **61**, 7199–7212.

POZRIKIDIS, C. 2011 *Introduction to theoretical and computational fluid dynamics*. Taylor & Francis Group.

PROSPERETTI, A. 1980 Normal-mode analysis for the oscillations of a viscous liquid drop in an immiscible liquid. *Journal de Mécanique* **19** (1), 149–181.

- RAMANAN, N. & ENGELMAN, M.S. 1996 An algorithm for simulation of steady free surface flows. *Int. J. Numer. Methods Fluids* **22**, 103–120.
- VIANA, F., PARDO, R., YÁNEZ, R., TRALLERO, J.L. & JOSEPH, D.D. 2003 Universal correlation for the rise velocity of long gas bubbles in round pipes. *J. Fluid Mech.* **494**, 379–398.
- WEATHERBURN, C.E. 1927 *Differential geometry of three dimensions*. UK: Cambridge University press, part 127, pp 251.